Peer-Reviewed Technical Communication

Safe Maneuvering Near Offshore Installations: A New Algorithmic Tool

Ilia Maslov, *Member, IEEE*, Elena B. Ambrosovskaya, Alexander M. Dvorkin, Anton V. Proskurnikov, *Senior Member, IEEE*, and Alexander Mordvintsev

***Abstract*—Maneuvers of human-operated and autonomous marine vessels in the safety zone of drilling rigs, wind farms and other installations present a risk of collision. This article proposes an algorithmic toolkit that ensures maneuver safety, taking into account the restrictions imposed by ship dynamics. The algorithms can be used for anomaly detection, decision making by a human operator or an unmanned vehicle guidance system. We also consider a response to failures in the vessel's control systems and emergency escape maneuvers. Data used by the algorithms come from the vessel's dynamic positioning control system and positional survey charts of the marine installations.**

***Index Terms*—Collision avoidance, marine safety, marine transportation, motion planning.**

I. Introduction

THE global energy sector critically depends on the operation of offshore assets, such as drilling rigs, production platforms, and fixed and floating wind farms (see Fig. 1). Service and maintenance of such installations employ a fleet of specialized offshore support vessels (OSVs) that are designed for low-speed maneuvers in the direct vicinity of the assets and are equipped with dynamic positioning (DP) systems.

The international rules [1], also imposed at national levels, establish an exclusion safety zone around the outer limits of the marine facilities that extend to 500 m. The entry to such a zone is restricted for any unauthorized watercraft as it may present safety and security risks. Once a vessel is chartered by the offshore asset operator and approved for entry, it becomes subject to requirements ranging from the redundancy level of critical equipment to the approach and departure sequences. These requirements, which are based on the lessons learned from incidents, may vary between the asset operators and can go into a significant level of detail [2]–[8].

Maneuver safety near offshore installations has many aspects and can be evaluated from different perspectives. Two key characteristics used to assess the damage caused by a collision are the energy absorbed by a marine installation and the impact impulse [9], [10]. Since these characteristics depend on the speed of the vessel at the time of impact, concentric safety regions around the installation are introduced (as explained in Section II), in which the vessel crew is prompted for a gradual speed reduction. Standard approaches to the offshore risk assessment [11], implemented in modern risk assessment software tools [11, Ch. 9], are based on the explicit estimates of probabilities and energies of collisions.

Although the maximum impact speed is specified [12] as 2 m/s, collisions at a much lower speed also present a risk of damage. A collision can render an OSV out of service if contact is made between the ship's navigation mast and the elevated topsides of a marine installation. This motivates an alternative line of research, which is concerned with the development of algorithms and software for real-time vessel's motion planning, fault-tolerant control and monitoring of the equipment reliability near an asset. The overall purpose is to diminish the risk of a collision resulting from a loss of station-keeping control.

To a certain extent, the latter problem is solved by DP systems, which are now considered as an indispensable part of a modern OSV's equipment and provide accurate position keeping and trajectory steering under changing environmental conditions. The recent progress in marine electronics, signal processing and control theory has facilitated the development of DP technologies and enabled the implementation of advanced filtering, control and fault-detection algorithms [13]–[17]. DP systems can provide some level of redundancy and eliminate faulty input data from sensors and other equipment. At the same time, DP control systems are not immune to incorrect motion planning and to operator's mistakes that may lead to accidents. To provide safety of a vessel and offshore assets, standard DP assurance procedures [18] are to be complemented with a standalone DP assurance software. Such a toolkit is able to assess the risk of accidents based on positional information pertaining to the serviced assets, the environmental conditions and the DP controller's output.

A prototype of a DP assurance tool has been created in collaboration between BOURBON Marine and Logistics and Navis Engineering Oy, named *DP Safewatch.*[1] This toolkit provides real-time monitoring of the vessel's equipment and assists the DP operator in maneuver planning and decision making, reducing the probability of accidents caused by the operator's mistakes. The operator can be a crew member interacting with the DP computer or, in the case of unmanned vessels [19] equipped with DP, a system that provides an interface between the motion planner and the DP controller.

The development of the DP assurance software involves a number of algorithmic problems. In this article, we focus on three key problems, studied in Sections II–IV: 1) computing and visualizing the *safety regions* within the 500-m zone, 2) fault consequence analysis, and

Manuscript received 11 March 2021; revised 14 November 2021; accepted 10 March 2022. Date of publication 1 June 2022; date of current version 13 October 2022. *(Corresponding author: Ilia Maslov.)*

Associate Editor: E. Brekke.

Ilia Maslov is with the BOURBON Marine and Logistics Head Office, 13007 Marseille, France (e-mail: ilia.maslov@gmail.com).

Elena B. Ambrosovskaya, Alexander M. Dvorkin, and Alexander Mordvintsev are with Navis Engineering Oy, 01740 Vantaa, Finland (e-mail: e.ambrosovskaya@navisincontrol.com; a.dvorkin@navisincontrol.com; a.mordvintsev@navisincontrol.com).

Anton V. Proskurnikov is with the Department of Electronics and Telecommunications, Politecnico di Torino, 10129 Turin, Italy (e-mail: anton.p.1982@ieee.org).

Digital Object Identifier 10.1109/JOE.2022.3159887

[1][Online]. Available: https://navisincontrol.com/news/dp-safewatch-successful-presentation-of-prototype-to-bourbon-marine-logistics/

(a)

(b)

Fig. 1. Offshore location: a marine installation and standalone obstacles. Photo courtesy of BOURBON Offshore. (a) Marine installation. (b) Buoys and a flare as standalone obstacles.

3) safe motion planning (particularly approaching the offshore asset and departure from the safety zone), respectively.

Safety regions (see Section II) are concentric areas around the marine installation whose boundaries correspond to predefined separation distances between the vessel and installations. International guidelines [6] impose various safety rules and procedures on a vessel entering a safety region; the DP assurance software alerts the operator in case of a violation.

Analysis of systems faults and their potential consequences (see Section III) is another important function of the DP assurance software. Each failure event (e.g., in actuators or the power plant) observable by the DP control system shall be mapped to a response or recommendation to the DP operator in accordance with reliability requirements [7], [20] and may prompt to avoid certain regions or to evacuate from the safety zone. This decision-making assistance is based on the fault tree analysis (FTA). The FTA is a general tool developed within the framework of statistical reliability theory, which has found many applications in transportation safety [21]–[25]. Blanke and Nguyen [17] give a holistic approach to modeling the effect of the failures on station-keeping in the DP vessels through a search of the minimum structurally overdetermined sets. It, however, requires an extended system of differential-algebraic equations describing the system's interactions between its components. The faults are injected and then residuals in the constraint parities aid in detecting and isolating. Blanke and Nguyen [17] establish the final metric as the position and heading excursions, thus, going beyond FTA's simplification. The method is dependent on the accessibility of the exact functional relationships for a range of equipment from multiple manufacturers and the corresponding control parameters are normally undisclosed by the makers. Model-based fault detection is implemented in a DP at a subsystems control level of the vessel in Fig. 10, and the alarms produced can be transferred to the fault tree as events. The approach proposed in [17] is theoretically impeccable and is likely to become a standard for defining failure mode and effect analysis (FMEA) for DP vessels in the coming years.

The third problem of the utmost importance is the motion planning (see Section IV), which includes planning not only optimal routes but also restrictions on the vessel's heading and speed. Optimal route planning in marine applications is nowadays well developed [26] (primarily, in the context of unmanned surface vehicles). Various approaches include deep reinforcement learning [27], artificial potential field [28], trajectory branching [29], Voronoi diagrams [30], iterative genetic algorithms [31], and grid-based methods such as fast marching [32], [33], Dijkstra [34], $A*$ and its modifications [35]–[37]. In this article, we propose a modification of the Dijkstra algorithm. Unlike most of the algorithms surveyed in [26], we take into account not only the geometry of obstacles but also time-varying environmental forces (estimated in real time) and the international safety rules specific for marine installations [4]. To the best of our knowledge, few publications mention the specific problem of maneuvering around an offshore installation [38], [39]. This article develops the results previously published in [40]. Finally, Section V concludes this article.

II. Safety Regions and the Imposed Limitations

Motion planning in the 500-m safety zone is subject to constraints applied to the operational mode, speed over the ground (SOG) and heading. The safety zone can be split into safety regions that can be static (determined by the position of a fixed marine installation) or dynamic (depending on the environmental forces affecting the vessel and updated in real time). A dynamic, or *drift-on*, safety region is an

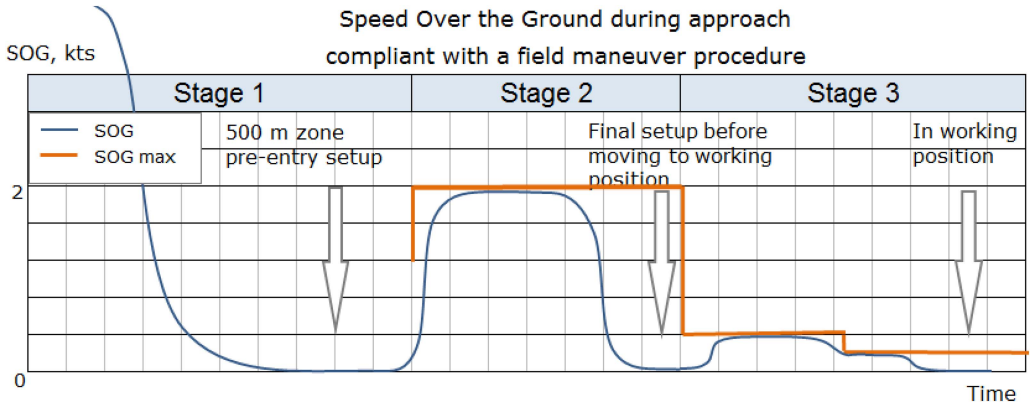

Fig. 2. SOG along the approach trajectory as intended by a set of field safety instructions.

area in which environmental forces tend to move the OSV toward the other offshore assets creating a risk of collision. The region can be defined by the projection of the asset geometry to the 500-m zone border in the direction opposite to the resultant environmental force. An allowance for the ship's own dimensions and inertia shall be made when estimating the boundary of a drift-on region. It should be noted that the computation of safety regions or safety maps is a prerequisite for guaranteed safe motion planning [29], [32], [41].

A trajectory of a supply vessel in a safety zone with several drift-on regions is shown in Fig. 3 with the corresponding speed and heading trends. The bridge team is required to consider all the dangers to navigation present in the 500-m zone when deciding upon an adequate maneuver. This includes flare booms extending from platform topsides, standalone flares, anchor patterns, submerged dangers, buoyage, export hose arrangements, and other elements of a marine facility. For an OSV engaged in supply, potentially dangerous objects can be categorized into the following:

1) Subsurface obstacle: No direct risk of collision, but passing through the region is prohibited, polygonal representation without a core object.
2) Surface obstacle: Direct risk of collision, the no-go area boundary is defined at a certain distance from the obstacle used as a core object.

Such objects need to be used as a basis for safety map generation in motion planning.

A. *Safety Zone Boundary Definition*

To guarantee that the vessel can maintain position and heading and is in every respect ready for the operation, the maneuver is split into three stages [4] that are illustrated in Fig. 2. The first stage covers the pre-entry checks and the initial estimation of the environment. The vessel's mathematical model is updated in order to estimate the DP current.[2] A drift test can also be carried out to assess the actual current. Vessel systems are set to the redundant configuration of the critical activity mode (CAM) [5]. Permission to enter is obtained from the marine installation. The second stage describes maneuvering inside the 500-m zone in Joystick mode. At the end of this stage, the vessel is brought for the final station-keeping test at 1.5-L distance or 2.5-L distance in a drift-on case, where L is the ship's length overall. The ship is set up in a fully automatic control mode. The vessel's mathematical model and DP current are updated again. The third stage covers the movement in a fully automatic mode to the working position, e.g., next to a crane of a platform. A preferred shape of the SOG trend in the segments with the maximum limits of 0.3 and 2.0 kn would be symmetric sigmoids to accommodate the setup verifications between the phase transitions, as presented in Fig. 2.

A human-operated maneuver is presented in Fig. 3. The SOG trend demonstrates several deviations from the prescribed set of rules, as given in Table I. The segments of the SOG trend in red correspond to SOG alarm state, where the limits of the regions along the trajectory are exceeded. We can observe that the operator has completed an initial setup of the first stage closer to the platform than expected, as indicated at 11:15:00 by a 10-min zero SOG segment. Then, the second stage's final setup took place again closer than expected at 11:35:00. Such deviations offer an area for improvement ranging from the decision support to the calculation of a recommended setpoint.

The guideline [6] defines the minimum steel-to-steel separation distance (MSD) for working with the offshore installations in correspondence with the ship's DP class. The station-keeping performance shall play a part in defining it. The external disturbance acting on the vessel, being the superposition of current, wave and wind forces, can be decomposed into the sum of low- and high-frequency components. We suppose that the low-frequency part of the disturbances is precisely estimated and compensated by the DP position controller, preventing the vessel's drift away from the setpoint. The ship's excursions from the setpoint are thus caused by the uncompensated high-frequency wave forces that can be approximated by the stationary Gaussian random process with a zero mean [43, Ch. 7]. A closed-loop system is formed of the vessel and its controller. Such a system can be considered as a linear time-invariant filter. The filter's outputs are vessel's longitudinal and transversal excursions, which are also stationary zero-mean Gaussian processes. Under such an assumption, a 15-min observation of the station-keeping quality during the DP setup will allow capturing the maximum deviations with a 95% probability corresponding to 2σ (where σ^2 is the variance of the distribution). For a fixed installation, an MSD represented by 6σ or 2×10^{-9} probability of a collision shall be considered as a baseline value. A vessel shall not approach any installation closer to DP operations.

The digital representation offers safety regions visualization, allows identifying their geometric overlaps and detecting the vessel's entrance into one of these regions. Digitalization of the above map objects requires the creation of several concentric regions within the 500-m zone

[2]The DP current is an internal estimate of the current arising in the algorithms of Kalman filtering [42]. As a current estimate, this estimate is typically not accurate since it accounts for more loads than currents, including the presence of additional slowly varying external loads and unmodeled dynamics for the vessel.

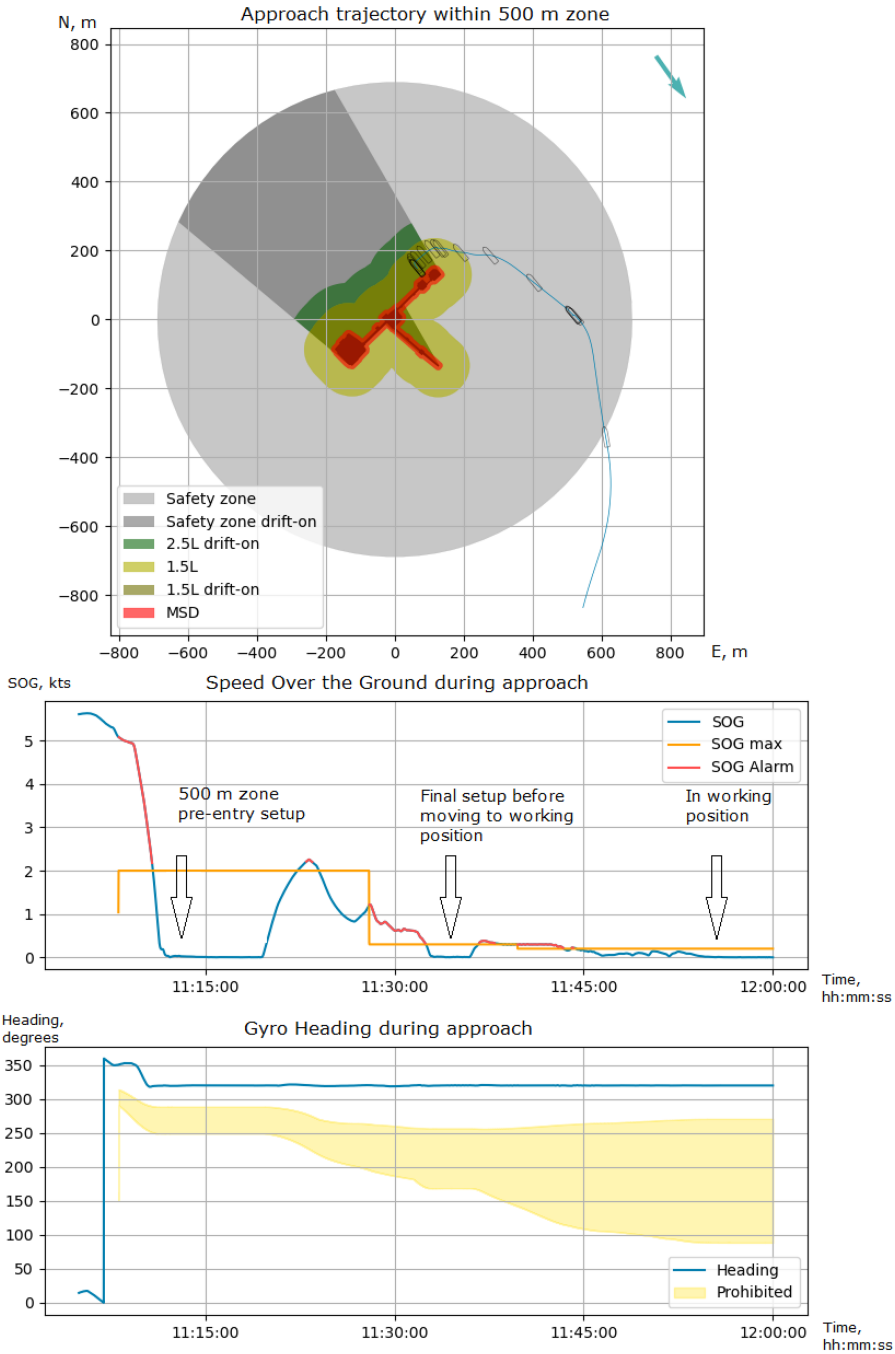

Fig. 3. Supply vessel maneuvers completed in a safety zone of marine assets. Maneuvers are performed by a human operator. The equivalent current's direction φ_{env} is 135°.

with varying requirements applicable upon entry. The safe trajectory problem is solved in a two-dimensional space of the marine assets. To comply with the recommendations from [4], the 500-m safety zone is split into the following characteristic areas:

1) drift-on region;
2) 1.5 ship lengths region (1.5 L);
3) 2.5 ship lengths region (2.5 L).

Additional regions can be introduced depending on the local field procedures, e.g., 20-m steel-to-steel as in the example. Rules are different for the regions with and without the drift-on collision hazard; an example is given in Table I.

B. Verifying Coordinate Transformation

The decision support system shall be capable of analyzing the map and ship's position relative to the installation in real time. Such an online analysis combines the DP system's output, including parameters of the vessel motion and the estimated forces, the installation maps and the geo-referenced limitations for the speed, heading and equipment configuration, as given in Table I. The necessary coordinate transformations are presented in Appendix A. Cartesian Local coordinate North–East (N-E) system is used for plotting. All absolute directions are measured from the North baseline.

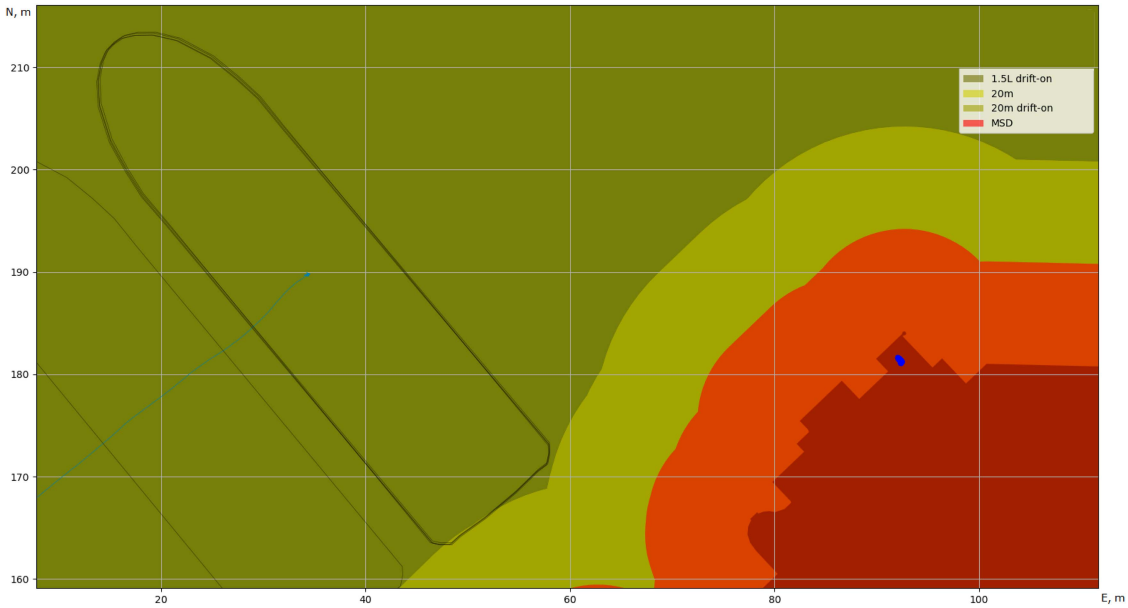

Fig. 4. Optic PRS Reflector position estimation (blue spot).

According to Table I, a vessel has to use a relative position reference system (PRS) based on an additional physical principle, i.e., optic or microwave measurement systems described in [44], to complement the satellite-based positioning, which is prone to signal masking and radio interference. Relative PRS measures distance and bearing from a ship to a reference point on a platform, a transponder or a reflector. We can then plot its absolute position by processing the output of the angular motion sensors and other PRS. In the example in Fig. 4, a reflector of an optic PRS is installed on the edge of the platform's topside, and the estimated position is marked by blue points. A bias can be determined by comparing the estimate with a known actual position. A variance can be calculated based on the distribution of the blue point samples. This task belongs to the offline processing of the DP data and may serve for the performance monitoring of the DP control system and PRS. Moreover, the detection and ranging sensors [45], [46] can be used to get the point cloud representation of the obstacles.

C. Online Estimation of Environmental Forces

For the calculation of the drift-on regions, an estimate of the average drift direction is needed, which depends on all disturbances acting on vessel. The total disturbance force arises as to the superposition of the aerodynamic force F_{aero}, the hydrodynamic force F_{hydro} and the wave drift force. The DP current, estimated by the DP system, absorbs the second-order wave drift, other unmodeled slow disturbances [42] and modeling errors in thrusters and hull dynamics. If we use the surface current measurements from a waverider buoy or a radar-based sensor, the wave drift force estimation needs to be added.

Figs. 5 and 6 show the above disturbance in the ship's and local NE coordinates. The mean environmental force F_{env} can be approximated as

$$F_{\text{env}} = F_{\text{aero}} + F_{\text{hydro}}$$

where

$$F_{x,\text{aero}} = C_{xa}(\gamma_a) S_{xa} \frac{\rho_a v^2_{\text{inflow wind}}}{2}$$

$$F_{y,\text{aero}} = C_{ya}(\gamma_a) S_{ya} \frac{\rho_a v^2_{\text{inflow wind}}}{2}$$

$$F_{x,\text{hydro}} = C_{xh}(\beta) L_{\text{WL}} T_m \frac{\rho v^2_{\text{inflow current}}}{2}$$

$$F_{y,\text{hydro}} = C_{yh}(\beta) L_{\text{WL}} T_m \frac{\rho v^2_{\text{inflowcurrent}}}{2}.$$

In the formulae, the following variables are used: inflow wind speed $v_{\text{inflow wind}}$, apparent wind direction γ_a, ship's SOG v_{SOG}, the DP current speed v_{current}, the DP current inflow speed $v_{\text{inflow current}}$, ship's drift angle β, transversal wind area S_{xa}, lateral wind area S_{ya}, mean draught T_m, waterline length L_{WL}, water density ρ and air density ρ_a. The aerodynamic (C_{xa}, C_{ya}) and hydrodynamic (C_{xh}, C_{yh}) curves' examples are shown in Figs. 7 and 8. Forces F_{aero} and F_{hydro} can be calculated using the same methods as for the vessel's capability plots [47].

The equivalent current direction φ_{env} can be determined experimentally in a drift test outside of the 500-m zone in which all thrusters are stopped for several minutes to allow the vessel to develop a speed from the forces exerted on the hull by the environment. When we power off all actuators and permit the vessel to drift, the course over the ground φ_{COG} will converge to φ_{env}. The speed through the water v_{STW} will fall to a value maintained by the wind and the wave drift.

This method of identifying the direction of the drift is not suitable for the final DP setup within the 500-m zone before moving to the working position because it requires uncontrolled motion. Instead, the calculated estimates shall be used together with the wind sensor outputs. A common approach in DP control systems is to estimate DP current direction continuously with an extended Kalman filter. To guarantee an accurate estimate, v_{env} is to be zero.

Table II illustrates an example of the drift direction estimated for a model of the supply vessel with parameters described in Table III. It should be noted that the wave drift is accounted for in the DP current estimate.

It is also possible to convert the force F_{env} with a direction ψ_{env} to an equivalent current with a speed v_{env} and an absolute direction φ_{env}. It is

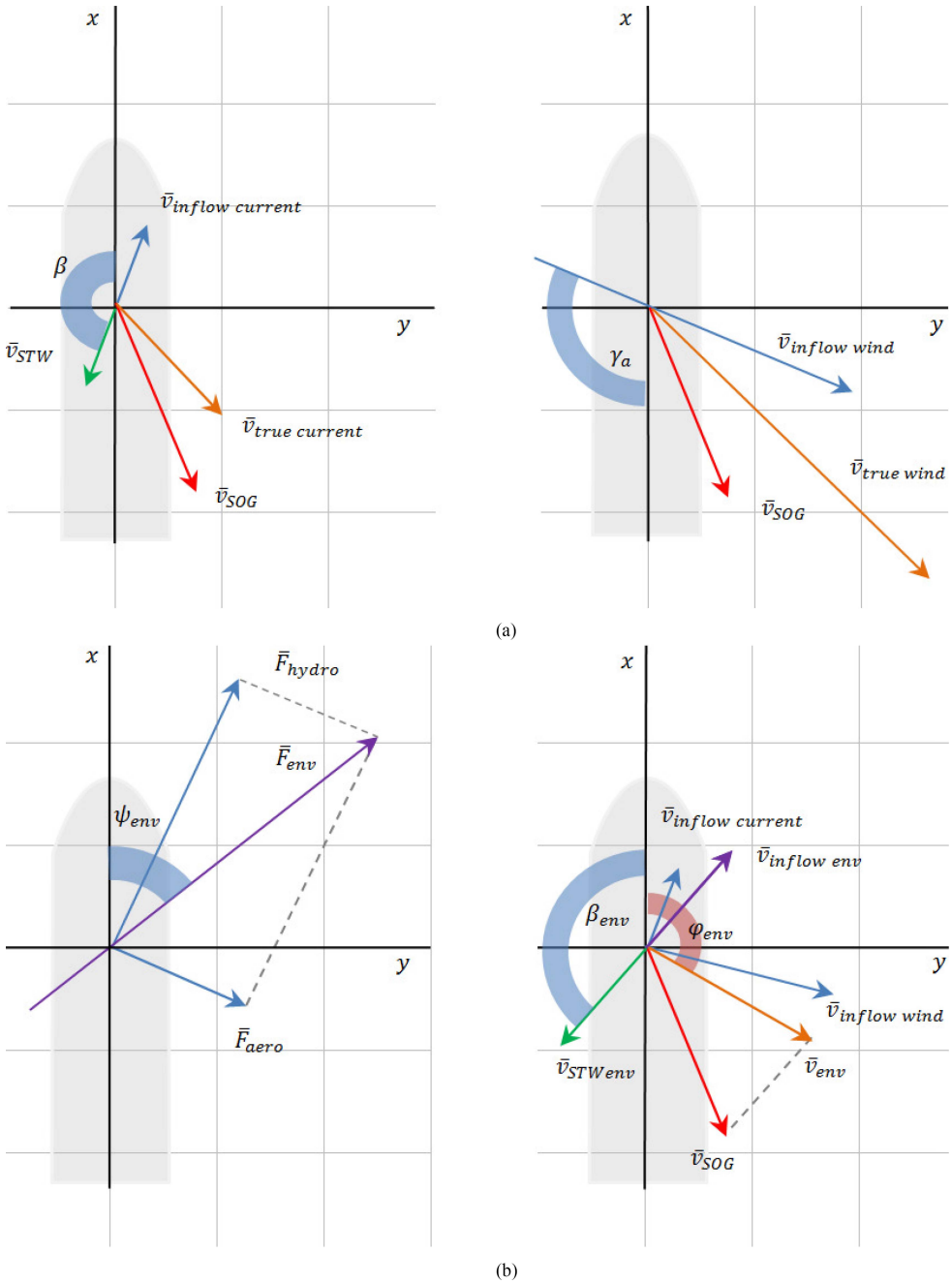

Fig. 5. Environmental disturbance in the ship's coordinates. (a) Wind (left) and current (right). (b) Forces (left) and the equivalent current vector (right).

required to solve the following system of equations for β_{env} and v_{env}:

$$\begin{cases} F_{x,\text{env}} = C_{xh}(\beta_{\text{env}}) L_{\text{WL}} T_m \frac{\rho v_{\text{env}}^2}{2} \\ F_{y,\text{env}} = C_{yh}(\beta_{\text{env}}) L_{\text{WL}} T_m \frac{\rho v_{\text{env}}^2}{2}. \end{cases}$$

Fig. 6 shows the resulting speed through the water vector $\overline{v}_{\text{STWenv}} = \overline{v}_{\text{SOG}} - \overline{v}_{\text{env}}$.

After establishing the drift direction, the drift-on regions can be plotted as a projection of the installation and obstacles geometry to the border of the 500-m safety zone. An angular margin can be added on the sides of the projection to account for the environmental variations around the averaged estimate.

While adequate and sufficiently long pre-entry setup permits the Kalman filter's (KF) estimates to converge to the reliable values, an automatic safety barrier is required in case of a mismatch between the model and the reality. It should account for a possible spatial variation of the surface current in the 500-m zone along the path and also for a bias due to any significant errors in the mathematical model of the ship's dynamics. In the underactuated regions, the force demand on the transversal propulsion is expected to be at a minimum without compromising the accuracy of tracking on the planned trajectory. As a safety barrier, we can define a threshold of 100% of the maximum transversal force of the less performant redundant group in a worst case failure scenario, which is coherent with the double redundancy and the fault tree described in Section III. If the actual propulsion output exceeds the threshold, then

TABLE I
EXAMPLE OF SAFETY ZONE LIMITATIONS FROM BOURBON DP OPERATION PROCEDURE (KN = KNOTS, L = SHIP LENGTH)

Region	Outer radius of a region	Maximum speed [kt]	Configuration	Relative PRS	Recommended Minimum control mode
Outside 500 m zone	More than 500 m	Maximum maneuvering speed	Any config	No	Manual
Around standalone obstacles	1.5L	0.5	CAM	No	Full auto
500 m zone					
Minimum Separation Distance (MSD)	10 m	No entry	CAM	Yes	Full auto
Between 500 m border and 1.5 L	500 m	2.0	CAM	No	Semi-auto
Between 1.5L and working position	1.5L	0.3	CAM	Yes	Full auto
500 m zone: Drift-on side					
Between 500 m border and 2.5L	500 m	1.0	CAM	No	Semi-auto
Between 2.5L and 1.5L	2.5L	0.5	CAM	Yes	Full auto
Between 1.5L and working position	1.5L	0.3	CAM	Yes	Full auto

a new station-keeping setup at $v_{\mathrm{SOG}} = 0$ kn is required. The KF will then converge to new parameters of the environment and the trajectory will be recalculated, eliminating the risk of a loss of control due to insufficient sideway thrust applied against an unmeasured disturbance.

III. FAULT CONSEQUENCE ANALYSIS. RESPONSE TO FAULTS AND UNDESIRED EVENTS

A ship's configuration can vary based on the distance to an offshore installation. This can include a specific setup of the PRS, of the power plant components online (generators, engines and energy storage systems) or of any valve, breaker or control system. An FMEA of a DP vessel compliant with [48] identifies the safest configuration against a single point failure. Such configuration is documented as CAM [5]. Then for an intact correctly functioning configuration, an emergency response table is defined, where a combination of faults or conditions triggers specific responses by the bridge team. Such a table is called an activity specific operating guideline (ASOG). The ASOG is required to be implemented onboard according to [3], its contents are defined in [5] and [7]. ASOG is supposed to be incorporated into the vessel-specific DP operations manuals as a paper-based document. An automated version gives advantages for mitigating a human mistake by decision support and offers remote monitoring of the DP activities. Decision support can close a gap with alarm misinterpretation by an operator [49], as well as eliminate the cases where the bridge team ignores the safety limits defined in ASOG [50].

In this article, compliance with the specified CAM is verified during the obligatory setup sequences. That task can be automated in a digital solution with component status checked when crossing designated distances around marine assets.

Abnormalities, external conditions, setpoint excursions, and failures are mapped by ASOG to the response actions of the bridge team [5]. The emergency response can be grouped into Blue, Yellow and Red levels of alert. The Red alert status is the highest level prescribing an immediate

TABLE II
ESTIMATED ENVIRONMENTAL FORCE DIRECTION ψ_{ENV}, EQUIVALENT CURRENT SPEED v_{ENV}, AND DIRECTION φ_{ENV}

γ_a, °	0	90	0	0	0	45	90	270	45	45
$v_{inflow\ wind}$, m/s	10	10	0	15	15	15	15	15	20	25
β, °	-180	-180	-90	-90	90	90	90	90	90	90
$v_{inflow\ current}$, m/s	0	0	0.7	0.5	0.5	0.5	0.5	0.5	1	0.5
ψ_{env}, °	180	270	88	108	251	262	270	83	266	257
φ_{env}, °	180	260	90	160	200	220	270	40	240	210
v_{env}, m/s	0.78	0.36	0.7	1.13	1.13	0.88	0.73	0.29	1.26	1.43

[2]The ship's v_{SOG} and heading φ are set to zero.

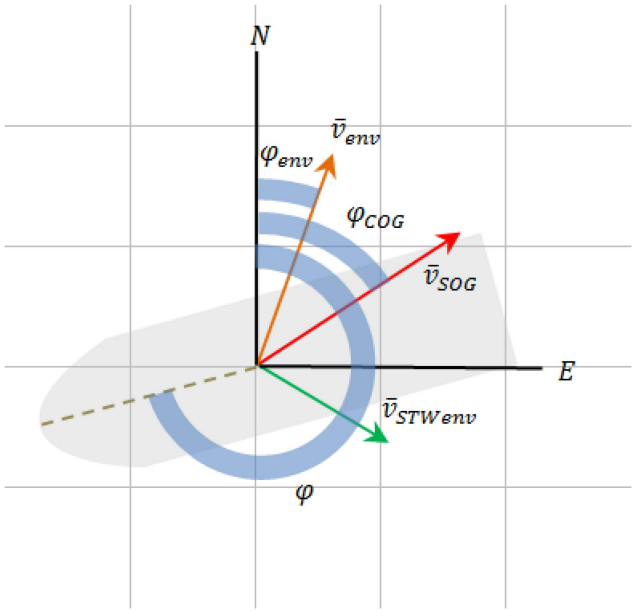

Fig. 6. Ship's motion parameters in the local NE coordinates.

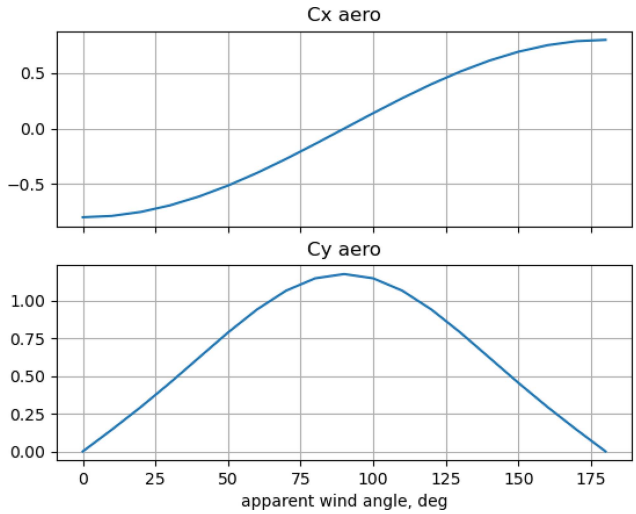

Fig. 7. Aerodynamic curves example.

TABLE III
SHIP PARAMETERS

Length overall, m	61.8
Displacement, t	2,886
Design draft, m	4.3
Transversal wind area, sq.m	174
Lateral wind area, sq.m	400
Maximum maneuvering speed, kts	8

evacuation from the safety zone. Based on the available industrial data inputs, a digital DP assurance application can prescribe a response to a fault or to an abnormality detected. A fault tree model with engineered controls can be used to link basic faults to the two catastrophic states that correspond to the Red status. Such connection is made through a top–down approach. The loss of the positional control can happen as a drive-off event, where the vessel is pushed off the desired position by active propulsion due to a software or sensor problem, or as a drift-off event, where the environmental force dominates the resultant thruster forces (typically due to a failure).

A simplified example of a drift-off event fault tree is given in Fig. 12 for a vessel described in Figs. 9–11. The generator and thruster status signals are linked to the undesired event at the top. To identify which ASOG alert status shall be specified to the basic initiating events, the nodes of the fault tree are given the color attribute based on the propagation algorithm. Starting from the top node, the color assigned changes when passing through a gate, as per Table IV. No probabilities are considered in this implementation.

That means that for a DP class 2 [3] system, a failure in basic event vertices will correspond to Yellow, as in Fig. 12, or Blue status given intact initial state of the double redundant system, where a loss of position and/or heading will not occur in the event of a single fault in any active component. A failure, detected in Fig. 13 as a Bow Thruster 2 basic event, changes the color for the branch up to the AND gate. It also triggers a Yellow ASOG status for the bridge team that is prompted to suspend any cargo operations. Then after updating the status in the top–down direction, "Bow Thruster 1 No thrust" is the last unchecked

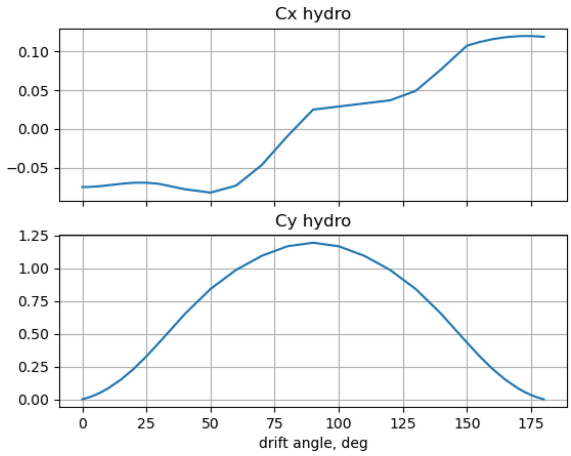

Fig. 8. Hydrodynamic curves example.

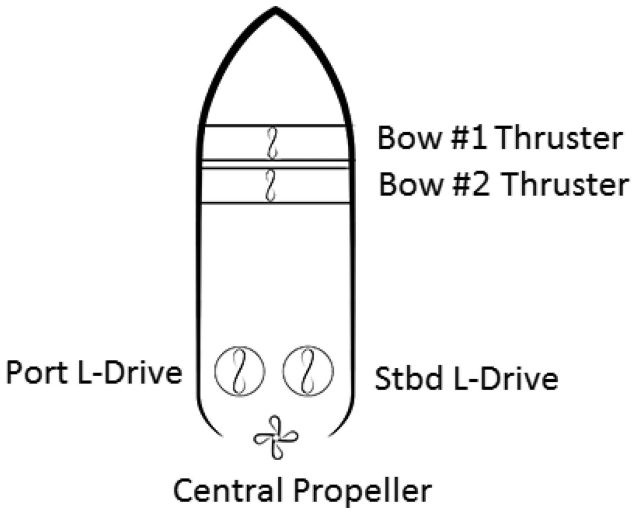

Fig. 9. Thruster configuration of Platform Supply Vessel *BOURBON Liberty 150* series.

TABLE IV
STATUS UPDATE RULE FOR THE SUCCESSOR NODES OF A FAULT TREE

Predecessor node status	OR	AND	Voting	Condition inhibit	Last unchecked in AND and Voting gates
Red	Red	Yellow	Yellow	Yellow	Red
Yellow	Yellow	Blue	Blue	Blue	Yellow
Blue	Blue	Blue	Blue	Blue	Blue

of the two nodes leading to AND gate; as a result, two basic events on its descendant branch get a Red attribute: "Bow Thr 1 Lost Ready Signal" and "Bus 1 Generator 1, 3 No power." Each of these two nodes becomes first-order faults or single-point failures as they are individually sufficient to cause the top drift-off event.

After automatically detecting an event, the operator will be informed about the change in the ASOG status and a delayed effect in case a timer is activated for any inhibits. For an unmanned vessel that would mean notifying the remote control center or automatically initiating an emergency escape maneuver.

IV. SAFE MANEUVER PLANNING

The bridge team shall follow the field operational procedures and the speed constraints are among the rules. Hence, there is an effect on the maneuvering duration. In the meantime, the offshore installation personnel encourages the vessel to approach faster to meet their own operational timeframe. Under pressure, the bridge team may take a shortcut against the established procedures. Close proximity time at the working location shall be kept to a minimum; therefore, the vessel shall only remain in the working location when supply operations are being carried out. That is why maneuvering in and out happens several times a day. Providing the bridge team with a digital tool to support the DPO's decision can help adhere to the procedures. The field operator can be directly involved in the process by setting the tool's constraints and the distances at which they are applied.

Such a direct involvement in the motion planning allows resolving safety and logistic issues more effectively. This, in turn, would relieve the pressure on the vessel crew performing the maneuvers. In this section, we propose an algorithm for the search of the optimal trajectory with a time of passage cost function on a field characterized by spatially varying speed constraints and minimum acceptable equipment configurations defined. The method develops the ideas previously published in [40].

A. Route Planning: Modified Dijkstra Method

A true North–East cartesian axis is used. The field area is split by the $m \times n$ sized grid Z with a resolution r, as it is shown in Fig. 14.

Any characteristic region is represented by a polygon, which is then rasterized on the cells of the Z grid with a resolution $r = 0.5$.

Each cell is attributed with logical *True* if the corresponding point of the vector mapping belongs to the characteristic region, or *False*, if not. Such a representation saves the CPU memory.

As a result, we obtain the following binary matrices of the same dimensions:

1) $Z_{500\,m}$—500-m zone;
2) $Z_{1.5\,L}$—1.5-lengths region;
3) $Z_{2.5\,L}$—2.5-lengths region;
4) Z_{Obstn}—area of all obstructions;
5) $Z_{\text{DriftOnSide}}$—drift-on region.

An example of a binary matrix Z visualization is shown in Fig. 15; pixelization depends on grid resolution r.

The shape of the drift-on region depends on the direction of the resultant environmental force estimated on the border of the 500-m zone as a part of the pre-entry tests. By using a linear combination of the binary matrices Z, a penalty weight can be assigned to every cell on the $m \times n$ grid in relation to the proximity dangers of each characteristic region. The grid can then be transformed into a graph by setting a rule of transit between the cells. To accelerate the computations, the number of vertices shall be reduced by decreasing the grid resolution by a factor k. This will simultaneously lead to accuracy degradation. It is reasonable to introduce a limit proportional to the size of the vessel, e.g., a quarter of the ship's Length overall (L_{OA}).

In the graph, we can further deduce the lengths of the edges and build the shortest path.

During the experiment, r was given as 0.5 m and $r_1 = rk$ as 15 m ($k = 30$). While going row-wise and selecting blocks of the size

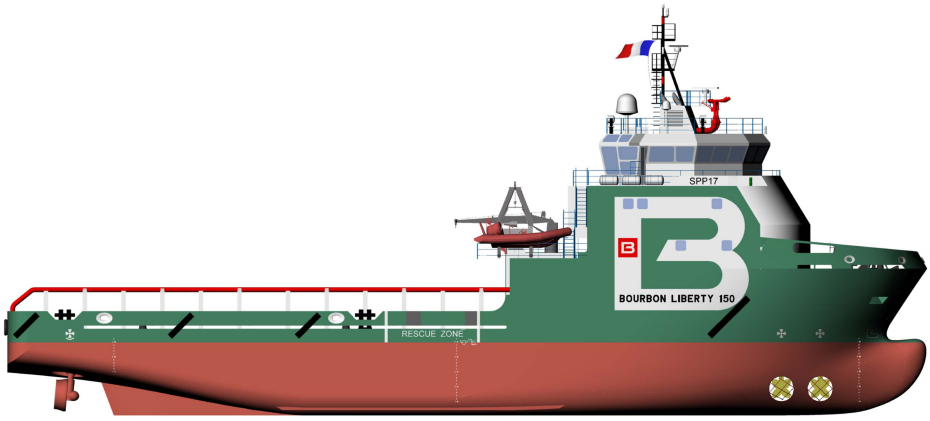

Fig. 10. Platform Supply Vessel *BOURBON Liberty 150* series. Image courtesy of BOURBON Offshore.

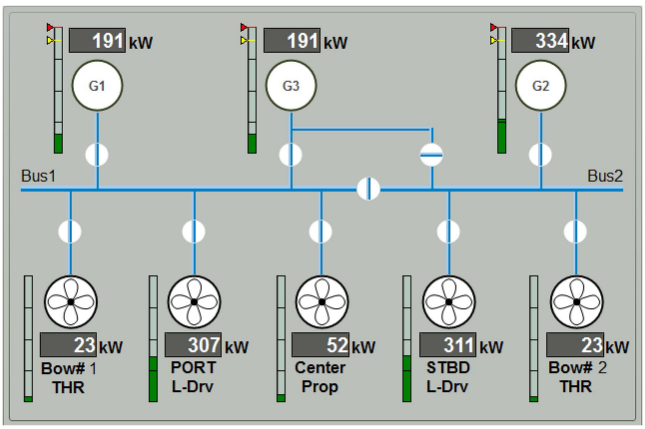

Fig. 11. Generators and the power distribution to thrusters on the Platform Supply Vessel *BOURBON Liberty 150* series. Screenshot of a DP Control system window. Image courtesy of Navis Engineering Oy.

$r_1 \times r_1$, we can calculate their total with the weights p, representing the close proximity dangers in each of Z areas.

With the distance from the installation, the weights shall decrease, and the permitted speeds shall increase. It is convenient to select the penalty p_Z as a function of the maximum allowed speed v_R in the particular region: $p_Z = 1/|v_R|$. Therefore, $p_{1.5\,L} > p_{2.5\,L} > p_{\text{DriftOnSide}}$.

The nodes pertaining to the region with the fixed marine assets are removed from the grid as no trajectory shall pass through (see Fig. 16).

Consequently, we will have a matrix W with a size $n/k = M$ by $m/k = N$, where the elements can be found as

$$W = \sum_{a=ik+1}^{(i+1)k} \sum_{b=jk+1}^{(j+1)k} \sum_{z \in zones} p_z Z(a,b).$$

Above i and j are the indices of rows and columns in the weight matrix. Zones Z are binary characteristic region matrices with the $ZObstn$ excluded.

For $k = 1$ (the same grid used for binary matrices and path building), all formulae will be simplified.

Hence, we calculate the weight of the elements of each augmented cell as a sum of all Z element weights contained in it.

TABLE V
EIGHT DIRECTIONS, 45° CONNECTION

Δi	1	0	-1	0	1	-1	1	-1
Δj	0	1	0	-1	1	1	-1	-1

It can then be normalized dividing by the penalty maximum

$$W_{\max} = k^2 \sum_{z \in \text{zones}} p_z.$$

As a result, we have mapped the rasterized chart into a penalty grid W (see Fig. 17).

We can now build a graph and draw the connections between nodes.

The graph edges are built, as shown in Fig. 18. The vertices will be linked in eight directions with a 45° step from the direction to true North corresponding to the nearest cell above. Table V represents the connectivity from a node. Length is $l = (\Delta i^{1/2} + \Delta j^{1/2})$ and weight is $\max\{W(i,j), W(i+\Delta i, j+\Delta j)\}$.

By moving row-wise, we verify the existence of the adjacent cells. The adjacent cells will be missing on the boundary of the grid and of the cells in Z_{Obstn}.

The edge weight between two incidental vertices can be obtained by multiplying the distance by the weight of the greatest corresponding W element. Thus, the penalty for passing through the characteristic regions will be equal to the time needed to pass the edge at the maximum permitted speed. Consequently, a search of the shortest path on such a graph conforms to the task of searching for the time optimal route without the ship's dynamic model constraints. We obtain a sparse matrix of a size $M^2\,N^2$, with every vertex having not more than eight incidental neighbors.

By knowing the first and the last nodes of the weighted nondirectional graph, we solve the task of finding the optimal route in Fig. 19 by the Dijkstra method [51].

An optimal solution is found in $O(V \log V + E \log V)$ steps, where V is the number of vertices and E is the number of graph edges. By taking into account not only 45° step directions, we can expand the graph adjacency according to Table VI (see Fig. 18). The result is shown in Fig. 20.

The simple A method is preferred over the modifications because the Bellman optimality is already proven, while the use of the heuristic functions, e.g., in $A*$, can accelerate the speed at the expense of omnidirectional efficiency. Due to considering

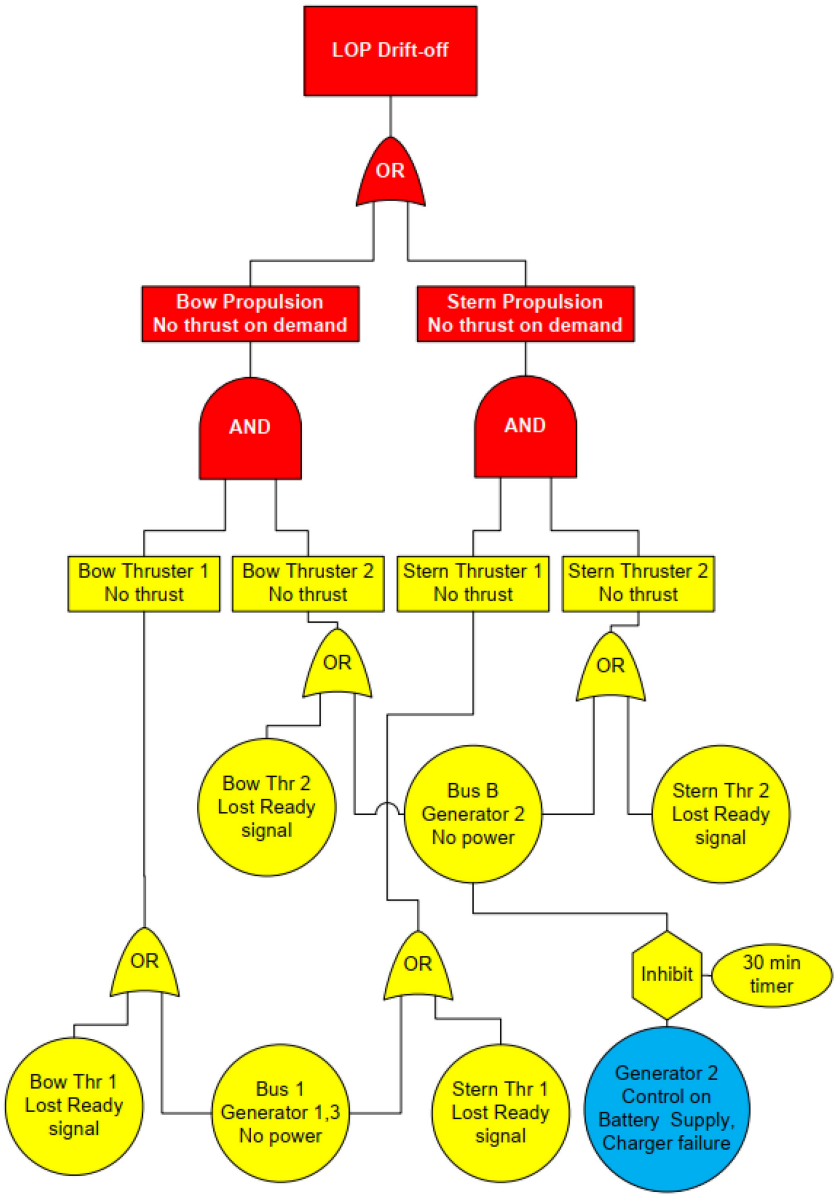

Fig. 12. Fault tree with ASOG status designated to basic events in the redundant intact state.

TABLE VI
16 DIRECTIONS, ADDITIONAL DIRECTIONS ONLY

Δi	1	2	-1	-2	1	2	-1	-2
Δj	2	1	2	1	-2	-1	-2	-1

only eight nodes per vertex, the computational speed is high; however, multiple resultant segments can be reduced to straight lines.

B. Visibility Check

The redundant nodes are further removed, where the substituting straight line does not collide with the obstacles and lies within the same region. Consider the shortest route D through a graph G on a scaled grid W. Map D to the original grids Z with a size of $n \times m$ depicting the characteristic regions around the platform.

We start by checking the first three elements in the sequence D. Provided that we can connect D_1 and D_3 by a straight segment without colliding with the region borders, the D_2 vertex can be viewed as redundant. Furthermore, we continue by considering D_1 and D_4, and verify if D_3 can be removed. Upon detecting a collision, the middle element is used as the first in the next loop, i.e., check D_3 and D_5, try removing D_5. A visibility check is implemented by an approximation method of Brezenham's line rasterization in the low-level programming for graphics. A vector line is plotted upon the Z arrays $n \times m$. Each of the line's pseudopixels has a *False* value superimposed on the Z. If Z changed after this operation, then a collision can be confirmed. This simple algorithm works with binary arrays, saves memory and boosts calculations.

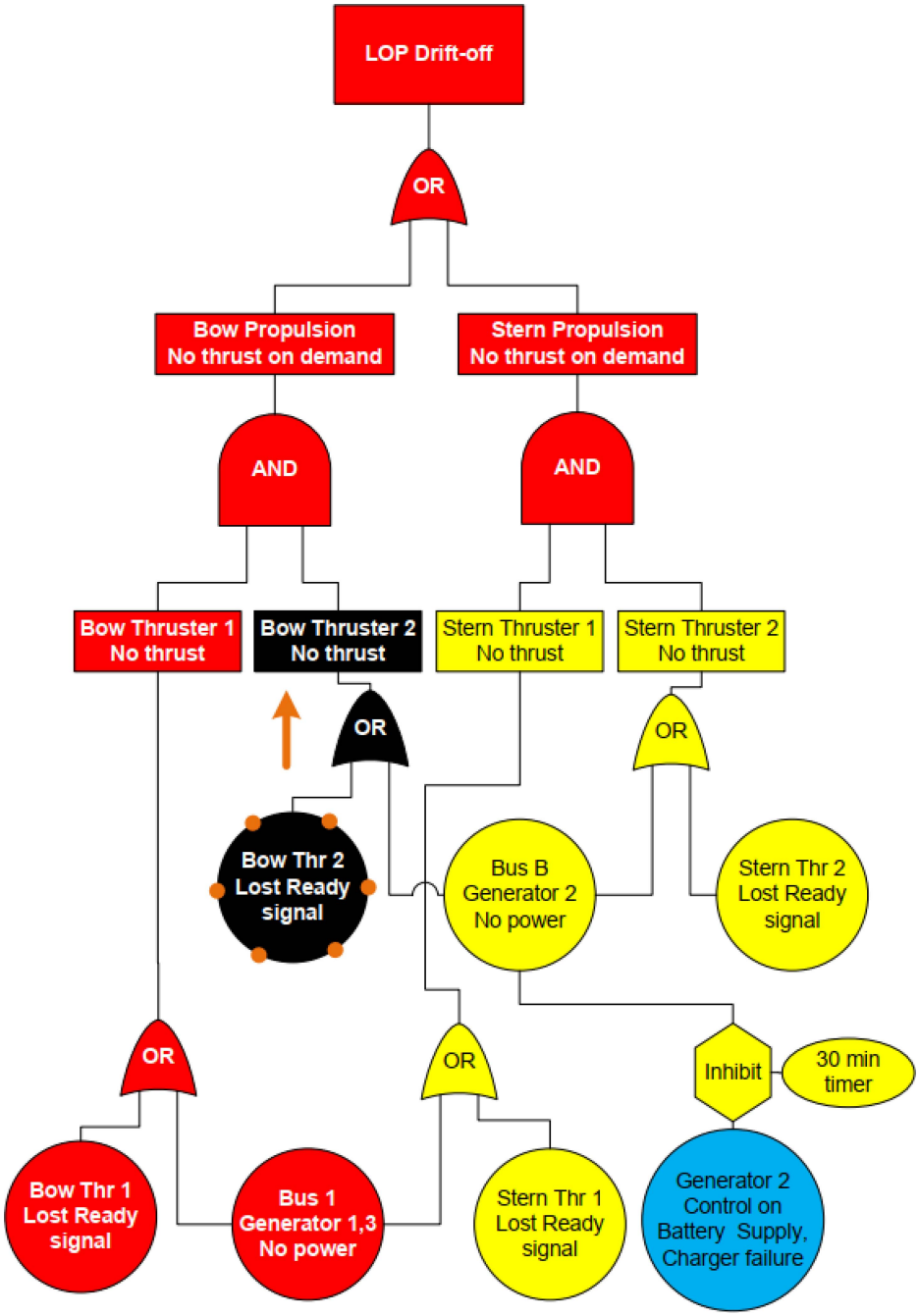

Fig. 13. Fault tree with updated ASOG status attributes following a basic event "Bow Thruster 2 loss of Ready signal." Yellow alert status has been passed to the operator and the node is now indicated as black.

If a collision is detected, two edges are not reduced to a straight line. While moving through the safety zone, Z has to reflect different characteristic zones, i.e., when considering edges in $Z_{2.5\,L}$, a different proximity region will act as the obstacle, the $Z_{1.5\,L}$. When verifying the edges in $Z_{1.5\,L}$, the collision detection algorithm will operate on Z_{Obstn}.

The resultant $D*$ route would be shorter than the original Dijkstra path if any pair of segments were replaced by a straight line. If no segments were replaced, the resultant path would be equal to the original sequence of points.

The complexity of this visibility check algorithm is defined by the number of vertices. A graph with n vertices will require $n-1$ iterations. Fig. 21 demonstrates an example of the visibility check on the nodes.

C. Restrictions on Heading and Speed in Drift-On Zone

OSVs working up-wind or up-tide of an installation in such a position that environmental forces tend to move the vessel toward the installation are at a higher risk of collision [52]. A digital solution

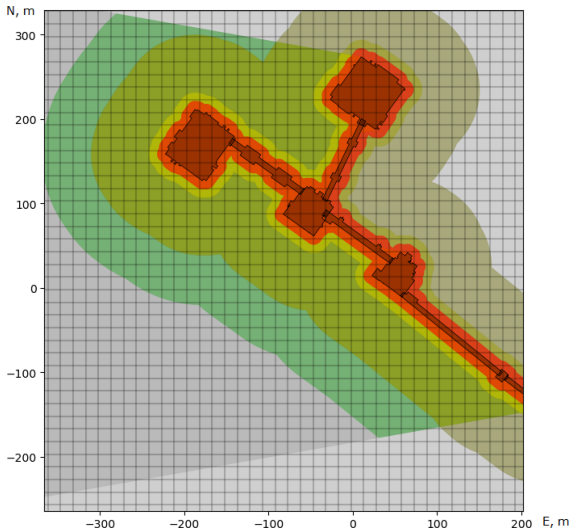

Fig. 14. Cartesian grid is superimposed on an offshore site with a 15-m resolution.

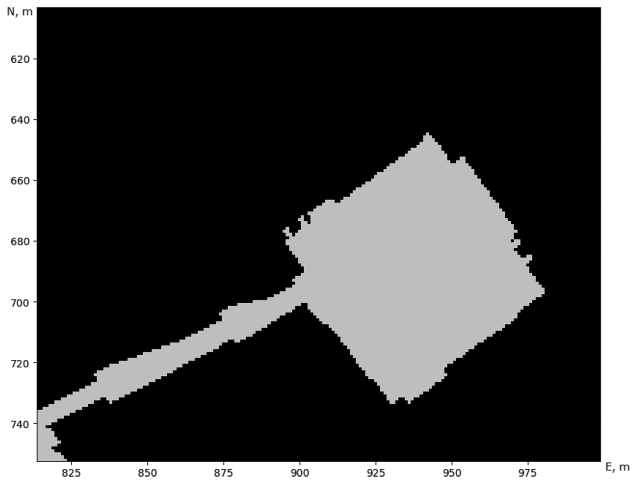

Fig. 15. Location mask matrix Z visualization, fragment.

shall be able to identify and demonstrate the drift-on region within the 500-m safety zone based on the estimated environmental factors. In the grid-based path planning algorithms, the reduction of exposure can be addressed by imposing a lower speed limit in the drift-on regions. This measure penalizes the trajectories passing through the drift-on region.

As per Table I, the maximum speed between the 500-m border and 2.5-L contour is 1 kn for the drift-on sector. In the drift-off region, at the same distance from the platform, the maximum speed is 2 kn. Subsequently, a penalty is twice as high in the drift-on sector than in the drift-off, and the calculated trajectories tend to bypass through the drift-off area and avoid the drift-on. Fig. 22 demonstrates 2000 trajectories plotted to 20 destination points within 1.5-L region with v_{env} directed at 225°. The upper right corner is a drift-on region, where the density of the trajectories is visibly lower.

For each segment on the route $D*$, the SOG and heading shall be selected according to Table I. To understand the limitations, we consider

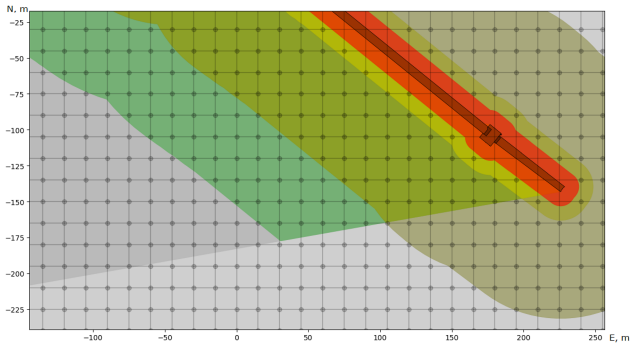

Fig. 16. Cartesian grid with resolution $r_1 = 15$ m, fragment with nodes.

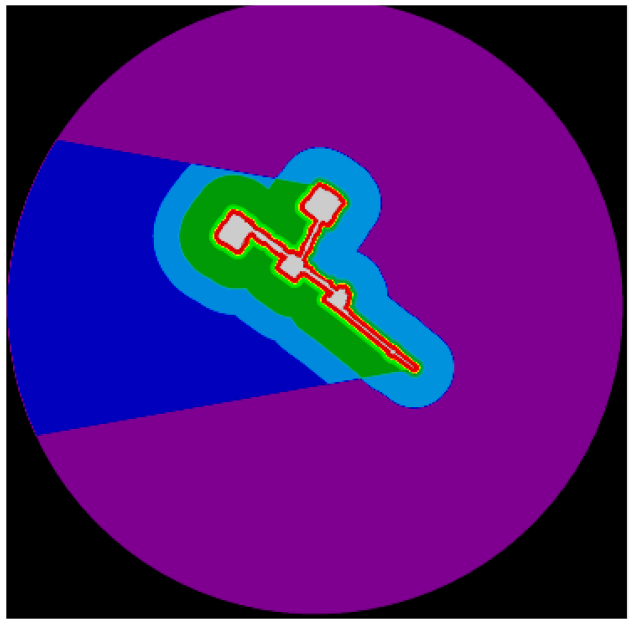

Fig. 17. Penalty grid W visualization presents the heatmap for a site composed of the regions defined in Table I.

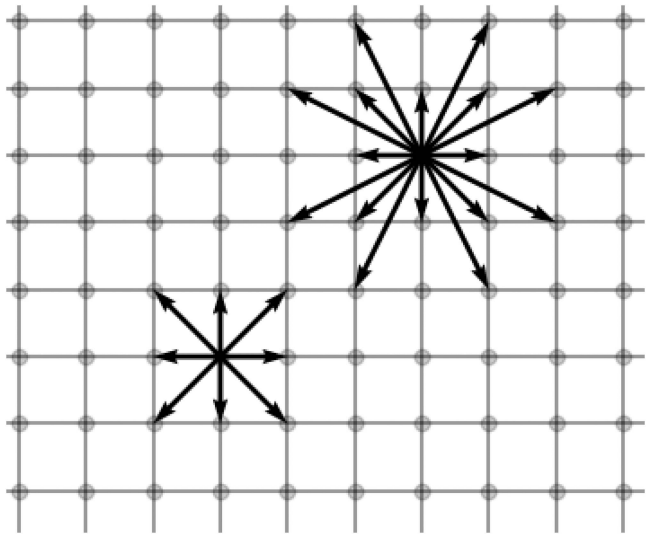

Fig. 18. Cartesian grid with path graph nodes connection principle.

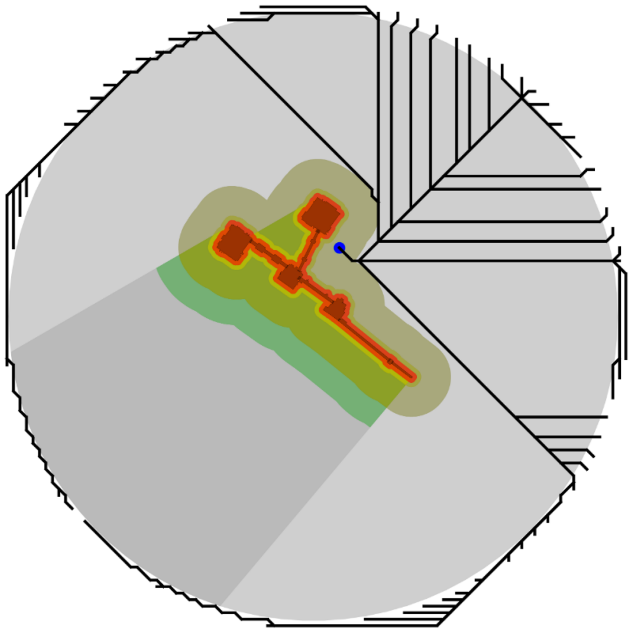

Fig. 19. Dijkstra method trajectories from different start points to working position (blue dot), eight possible directions.

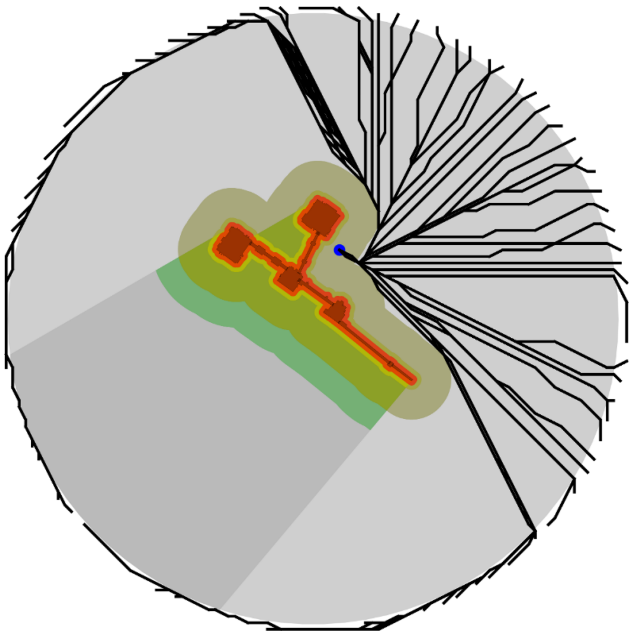

Fig. 20. Dijkstra method trajectories from different start points to working position (blue dot), 16 possible directions.

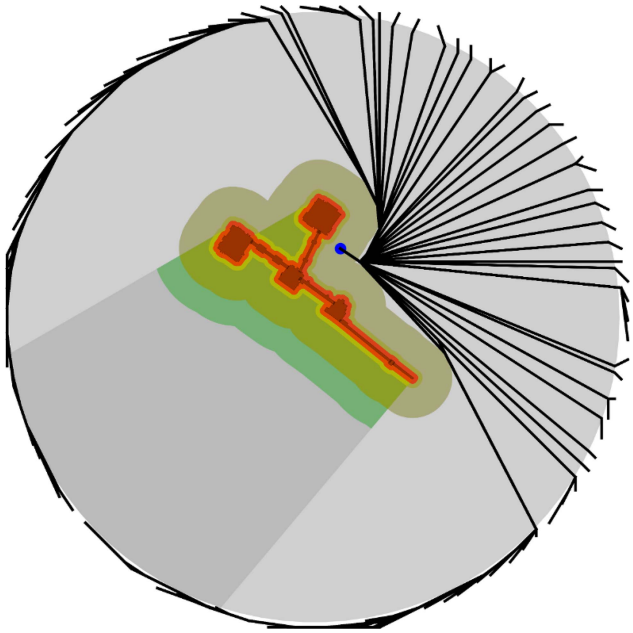

Fig. 21. Trajectory after removal of the redundant nodes, approaches to the position marked blue.

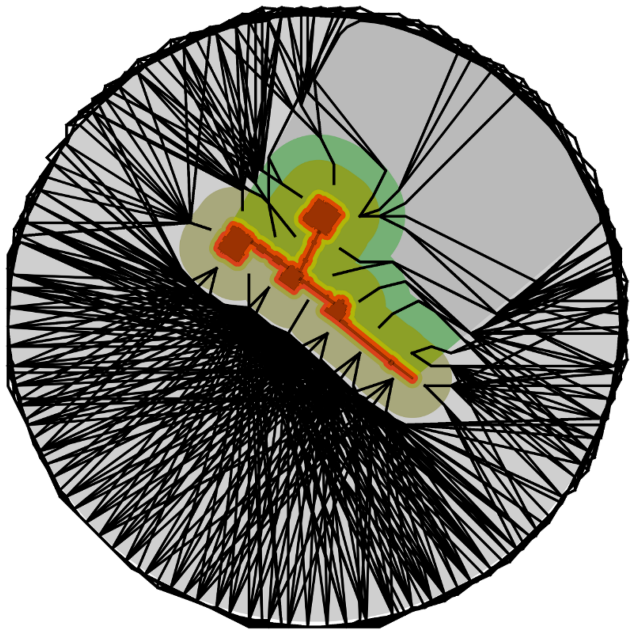

Fig. 22. Result of plotting 2000 approach trajectories with a uniform node connectivity, 16 neighbor node reach, $\varphi_{\text{env}} = 225^{\circ}$.

cases of drift-on and drift-off approaches to the working position under a platform crane.

Existing industry guidelines do not prescribe the choice of heading, except for the fact that it is not recommended to proceed with a bow directed toward the platform [4] when approaching the location.

A heading on each segment of the trajectory should be derived from the final working heading, which is subject to the position of the cargo on deck, crane boom length, current, and speed. If a cargo is located in the aft, the bow is normally directed away from a platform in the final working position. Backstepping from the final planned heading and knowing the region boundaries permits one to establish the sequence of headings on the route with a smooth transition between the segments.

In the following, we introduce additional restrictions to reinforce safety for maneuvers in strong currents. The goal of the limit is to guarantee that a vessel can reduce the SOG to zero by means of the active propulsion following the worst case failure event on any segment in the drift-on regions. We can view the vessel as fully actuated in the low-speed maneuver regions and as an underactuated control object [51] in the areas where a higher speed profile is needed.

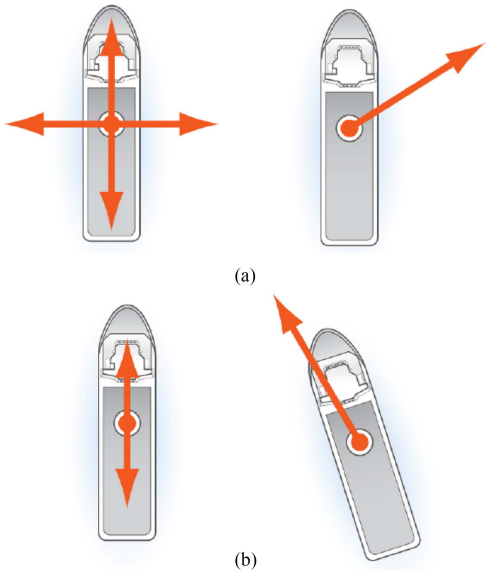

Fig. 23. Fully actuated mode versus underactuated mode. (a) Fully actuated vessel: thrust in all directions is possible. (b) Underctuated vessel: only ahead/astern motion with thrust applied in a limited angle from the ship's centerline.

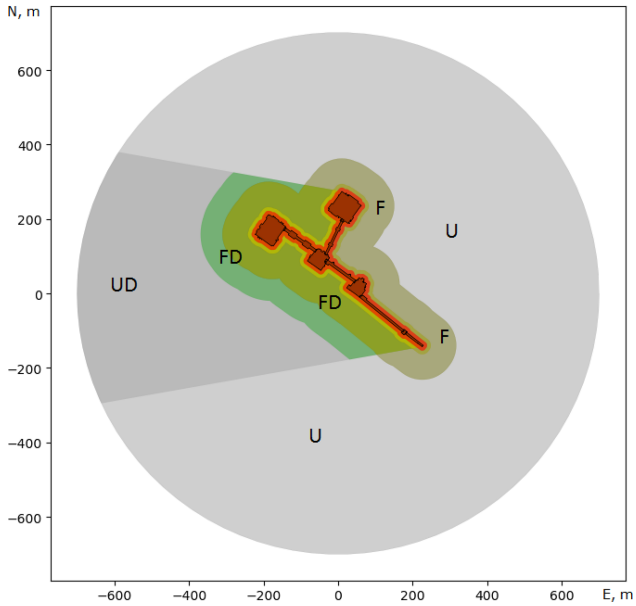

Fig. 24. Regions where the motion control is fully actuated (F, FD) and underactuated (U, UD).

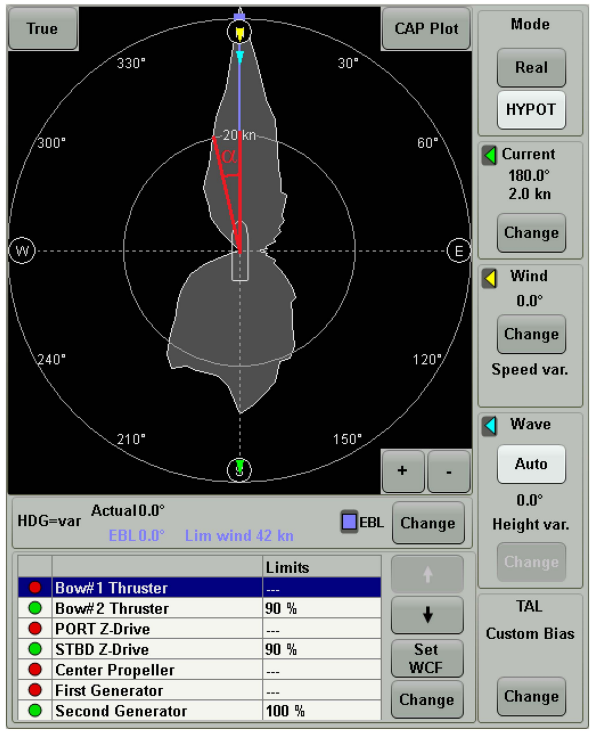

Fig. 25. DP capability diagram for WCF (a screenshot from Navis NavDP 4000 workstation [53]).

In the underactuated mode [see Fig. 23(b)], the bow thrusters are not used and the vessel is steered by means of the stern propulsion. That implies the following restrictions: $|\varphi - \varphi_{\text{STWenv}}| < 30^\circ$ and $|\varphi + \pi - \varphi_{\text{STWenv}}| < 30^\circ$. This mode is energy efficient as the low drift angle β provides less resistance, considering the similarity of a ship's hull's shape to an airfoil. The underactuated mode is normally used for transit. The change in the trajectory is achieved by altering the heading φ and the speed through the water v_{STW} (see Fig. 6).

In the fully actuated mode [see Fig. 23(a)], both bow and stern thrusters are used. φ_{STWenv} is not restricted with regard to φ. The motion in all directions is possible without a heading alteration but at a low v_{STWenv} (see Fig. 6). The bow tunnel thrusters are a common design feature in OSVs. The efficiency of these thrusters significantly decreases at a speed through the water beyond 3 kn.

Fig. 24 shows the regions where the motion control is fully actuated (F, FD) and underactuated (U, UD). The direction of each segment plotted by the algorithm is a course over the ground φ_{COG}. φ_{COG} is obtained from a vector sum of the speed through the water and the sea current. The drift-on (-D) regions are denoted as FD and UD.

In the U and UD regions, a change in the direction of the speed through the water requires heading alteration. In the F and FD regions, the direction of the speed through the water can be changed while maintaining the same heading by means of the sideway thrust.

In the UD and FD regions, heading restrictions are imposed. It is especially important if the maximum speed through the water sideways is less than the current. If that is the case and the relatively strong current is acting abeam, a collision cannot be prevented by operating the propulsion sideways only.

The heading limits are derived from the online capability plot and the worst case failure weather envelope contour in particular. This capability contour is defined by the remaining power and propulsion following the critical failure event. The contour represents the set of conditions where a balance between the ship's thrust and the environment is achieved with a variation in the wind speed. In Fig. 25, at the 20-kn wind radius, the capability plot defines two ranges of headings on which a position can be maintained given the environmental disturbance. From the two ranges, the minimum angle α between the axis of the weather envelope and the edge of the range can be taken as the safety limit for UD region and further imposed on the heading selection.

The headings on the path segments in UD region fit the range of

$$\begin{cases} |\varphi_{\text{env}} - \varphi| < \alpha, & \text{bow in the direction of the equivalent current} \\ |\varphi_{\text{env}} - \varphi + \pi| < \alpha, & \text{stern in the direction of the equivalent current} \end{cases}.$$

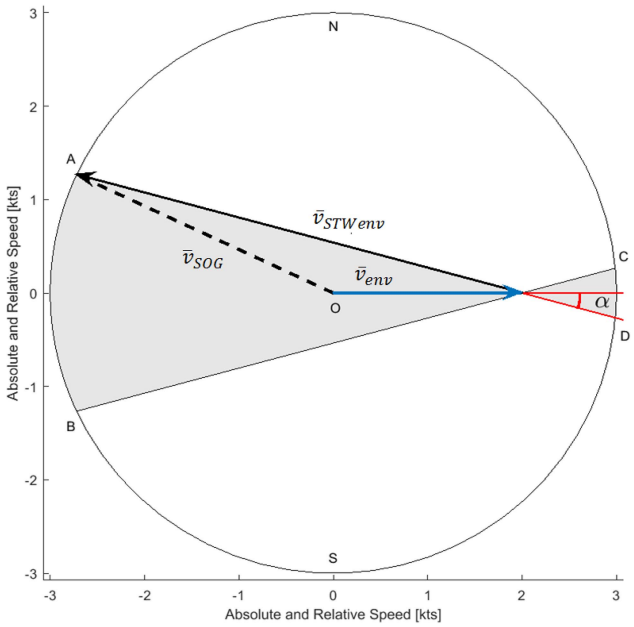

Fig. 26. Polygon in gray denotes the boundaries of allowable SOG with the heading restrictions applied. The φ_{env} is 90°. Maximum SOG is set to 3 kn in this example. v_{env} is the equivalent speed vector derived from F_{env}. All vectors are applied at the ship's center of mass.

Given the heading limit α, known direction of the current and the maximum permitted speed, we can map these limits into the restrictions on the course over the ground, which, in turn, will be equivalent to restricting the direction of the grid edges in the UD region. Fig. 26 provides an example. The angle α is used to plot the vectors of the maximum speed through the water in clockwise and counterclockwise directions from the axis of the current. The angles AOB and COD become the limits for the course over the ground. The edges plotted in the UD region shall remain in these ranges: AOB for the up-current direction of passage; COD for the down-current motion. The algorithm iterates over the nodes on the border of UD, takes them as source nodes, then identifies the target nodes on the other side of the border within AOB and COD sectors. This way only the valid edge directions are introduced in the grid for the UD region. In case the motion planning task is solved from within the UD region, the AOB and COD sectors are plotted from the initial position in up-current and down-current directions.

By maintaining a restriction in UD on α, a vessel will not experience a situation where on a low-speed maneuvering segment the trajectory control is lost due to insufficient sideway thrust. Moreover, after swiftly altering the course to align the ship's centerline with the resultant environment, the stern thrusters can be utilized to stop the vessel almost momentarily by a kick of longitudinal force. The stern azimuthal thrusters are the most performant by design, fit to propel the vessel on the interfield transits, this strategy optimizes their use for emergencies.

In the UD region, we can use a set of edges given in Fig. 18 only in the directions collinear to the current direction or with a difference within a prescribed value. However, when the number of possible directions is limited and the current's direction is not a multiple of 45°, then the result is not adequate. For the UD region, we suggest introducing a special connectivity of the boundary nodes.

Fig. 27 shows an example of a regular grid nodes' connectivity with the boundary nodes of drift-on region. An up-current sector is demonstrated. A connectivity from the arbitrary point is given. Results of route planning are presented in Figs. 28 and 29. To calculate the maximum v_{SOG} on a segment, we plot the $\overline{v}_{\text{SOG}}$ vector in the direction of φ_{COG} to find the intersection with the maximum speed polygon (gray) in Fig. 26.

The resultant trajectory is ready for use with the already existing low-speed motion control systems. On the underactuated segments, the heading and the longitudinal speed are manipulated, while fully actuated parts make use of the transversal speed in addition to the above. It should be noted that in the U region, the heading restrictions are lifted as a loss of active thrust will not result in a collision because it is a drift-off area. In both U and UD regions, the vessels can be maneuvered based on the line-of-sight algorithm given in [54] based on the environmental estimates of Section II.

The ASOG status, determined according to Section III, should be used as an input for the grid generation. If at any moment the vessel reaches the Yellow or Red alert, then all the nodes and edges representing the drift-on regions (UD and FD) shall be removed from the calculation. That would prevent a vessel from passing through a region when the redundancy in the critical systems has been lost. An exemption can be made for ASOG alerts linking to the relative PRS in U and UD regions. Such PRS need a close range for initialization, and with regard to them, the field rules may permit a lower requirement for redundancy for the period of approach or departure from the site.

D. Escape Maneuver

An escape route shall be identified from the working position to a safe area outside of the 500-m zone. The trajectory generator can produce escape routes to follow when making a routine or emergency departure from the marine assets. A digital solution needs to be able to plot the escape route and to update it regularly. The bridge team needs to be alerted if the path is being obstructed, or if environmental conditions changed to such an extent, that it significantly deviated from the last proposed trajectory. The cost function shall ensure the quickest time to escape the 500-m zone and, for an emergency escape, it shall take into account the remaining propulsion following a failure event. In Fig. 30, examples of the emergency escape trajectories are plotted. The restriction is lifted to allow leaving the drift-on region in a minimum time. The escape route generation can be coupled with the ASOG status change algorithm described in Section III. As both Yellow and Red conditions prompt for an evacuation with a different level of urgency, the escape trajectory acts as an important decision support for the bridge team.

E. Simulation Results

The algorithm has been tested to build trajectories between 100 points on the border of the 500-m zone and 20 destination points at 45 m from an offshore installation. Both sets are equally distributed along the perimeter of the corresponding geometries. The equivalent current φ_{env} is directed at 50°. A total of 2000 trajectories, built in each case, are denoted by a row in comparison Tables VII– IX. The time was measured with a prototype in Python; NetworkX library was used for the resultant graph handling. Increasing the grid resolution affects the computational time; however, 15-m value is deemed to be suitable for the dimensions of the vessel used as an example in Fig. 10. The length of the computed trajectory is divided by a straight distance, between its beginning and the end, to produce a normalized distance L/L_0. The

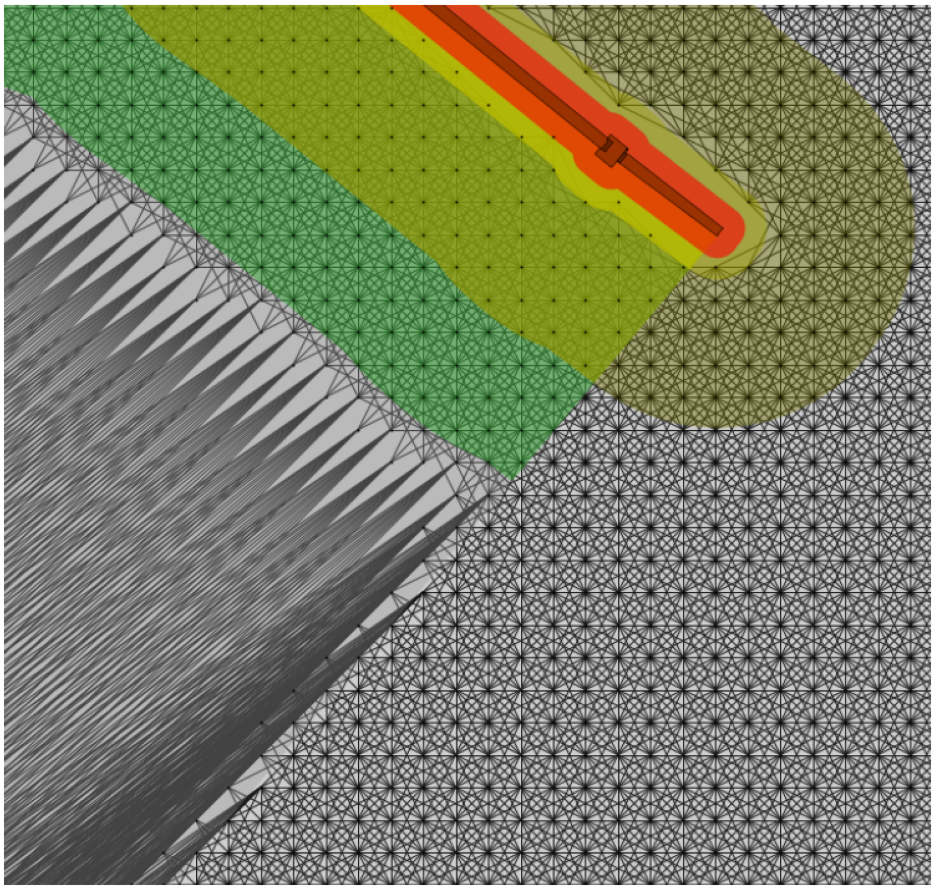

Fig. 27. Cartesian grid with resolution $r_1 = 15$ m, fragment with nodes (strong current).

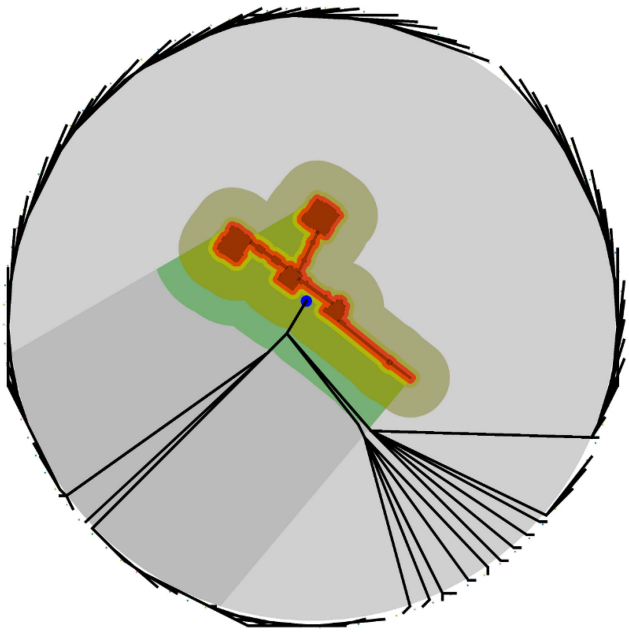

Fig. 28. Trajectory with strong current limitations imposed, approach to a drift-on working position (blue dot).

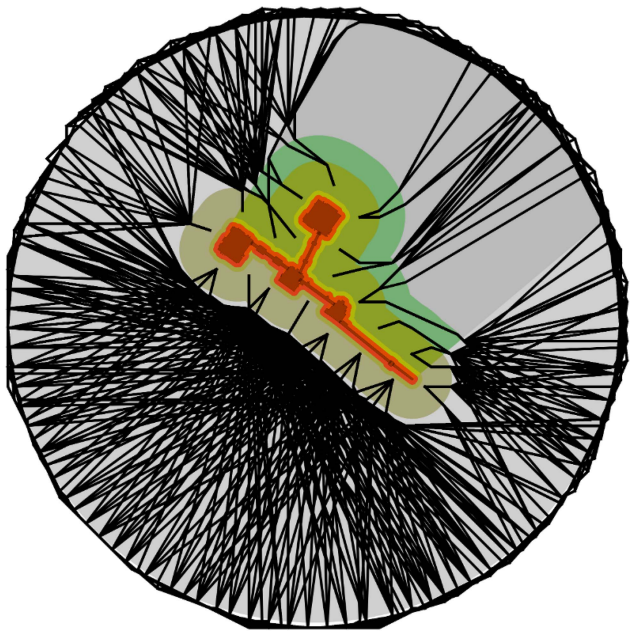

Fig. 29. Result of plotting 2000 approach trajectories with a connectivity method described in Section IV-C for the UD region, 16 neighbor node reach, $\varphi_{\text{env}} = 225\,^{\circ}$.

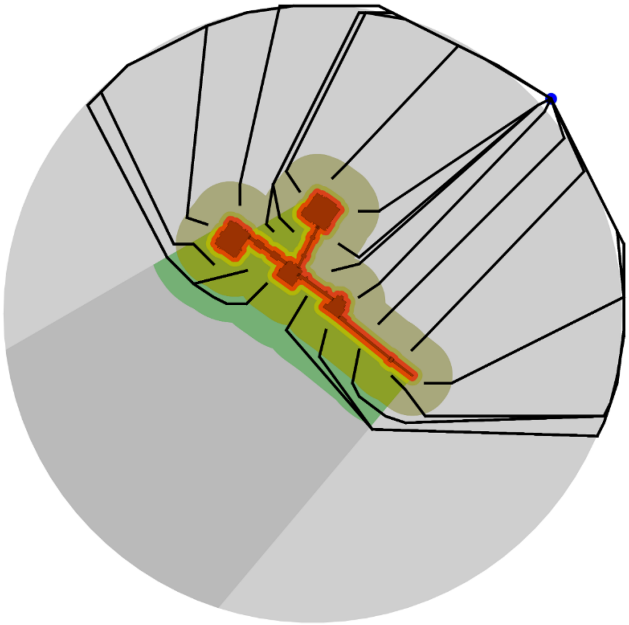

Fig. 30. Escape maneuvers to a safe position (blue dot).

TABLE VII
ALGORITHM COMPARISON TABLE FOR A 15-M GRID RESOLUTION

r_1 = 15 m	L/L_0	T comp [s]	Nodes	Edges
Drift-on region				
8 neighbour nodes and UD sector	1.763747	1.220938	9 698	42 760
16 neighbour nodes and UD sector	1.802033	1.906858	9 698	79 351
8 neighbour nodes and uniform connectivity	1.735860	0.895884	11 084	43 524
16 neighbour nodes and uniform connectivity	1.769143	1.734191	11 084	86 261
Drift-off region				
8 neighbour nodes and UD sector	1.615878	1.213366	9 698	42 760
16 neighbour nodes and UD sector	1.567935	1.899680	9 698	79 351
8 neighbour nodes and uniform connectivity	1.615878	0.883967	11 084	43 524
16 neighbour nodes and uniform connectivity	1.567935	1.710215	11 084	86 261

TABLE VIII
ALGORITHM COMPARISON TABLE FOR A 12.5-M GRID RESOLUTION

r_1 = 12.5 m	L/L_0	T comp [s]	Nodes	Edges
Drift-on region				
8 neighbour nodes and UD sector	1.731165	2.085753	14 097	62 714
16 neighbour nodes and UD sector	1.759783	2.792663	14 097	116 433
8 neighbour nodes and uniform connectivity	1.716007	1.250059	16 170	63 700
16 neighbour nodes and uniform connectivity	1.751131	2.459592	16 170	126 447
Drift-off region				
8 neighbour nodes and UD sector	1.643819	2.070612	14 097	62 714
16 neighbour nodes and UD sector	1.575044	2.772441	14 097	116 433
8 neighbour nodes and uniform connectivity	1.643819	1.231102	16 170	63 700
16 neighbour nodes and uniform connectivity	1.575044	2.442925	16 170	126 447

TABLE IX
ALGORITHM COMPARISON TABLE FOR A 10-M GRID RESOLUTION

r_1 = 10 m	L/L_0	T comp [s]	Nodes	Edges
Drift-on region				
8 neighbour nodes and UD sector	1.754492	3.110446	21 949	98 173
16 neighbour nodes and UD sector	1.785646	4.854190	21 949	182 620
8 neighbour nodes and uniform connectivity	1.727464	2.002947	25 265	99 835
16 neighbour nodes and uniform connectivity	1.759946	4.125577	25 265	198 474
Drift-on region				
8 neighbour nodes and UD sector	1.603813	3.097478	21 949	98 173
16 neighbour nodes and UD sector	1.577498	4.824412	21 949	182 620
8 neighbour nodes and uniform connectivity	1.603813	1.972247	25 265	99 835
16 neighbour nodes and uniform connectivity	1.577498	4.084344	25 265	198 474

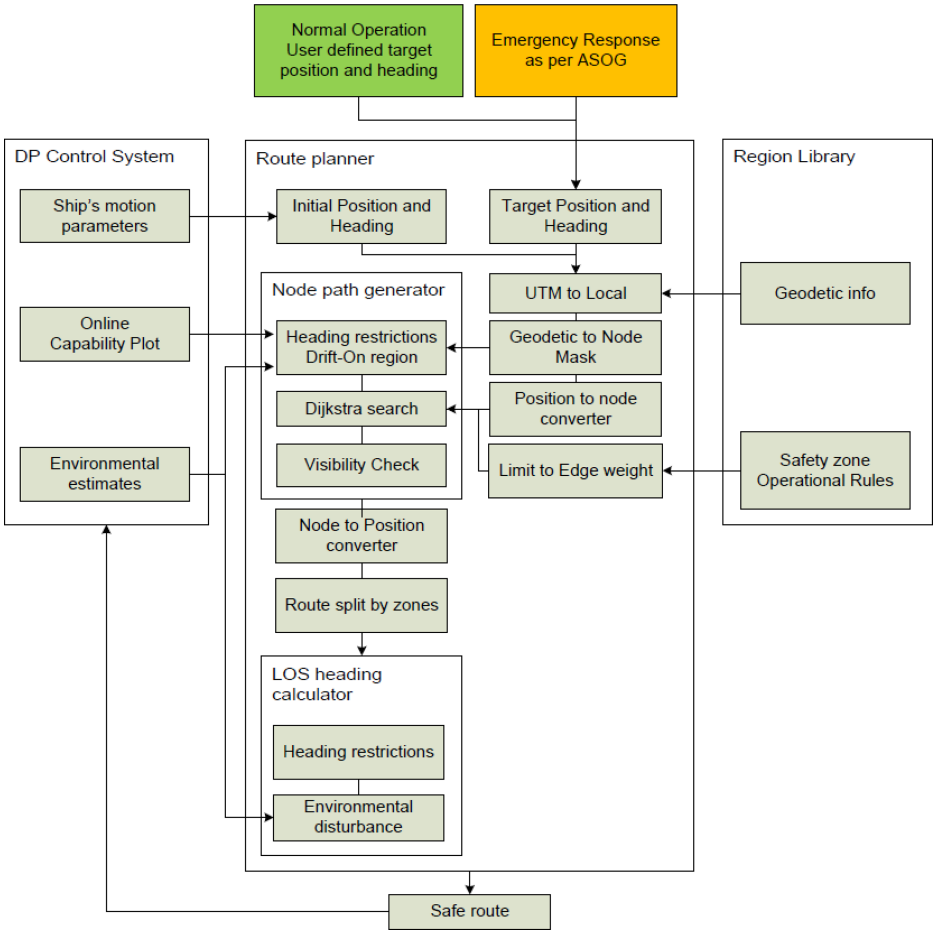

Fig. 31. Overview of the safe maneuver planning algorithm.

method for handling UD region, as decribed in Section IV-C, increases the computational time up to 5% and is considered to be feasible. This method uses approximately 10% less nodes; this feature corresponds to their removal in UD regions.

For a field application, the code can be optimized, while on a 15-m grid, the time delay is already acceptable being less than 2 s, as in Table VII.

V. Conclusion

This article proposes a solution for safe maneuvering at marine assets as a combination of tasks. Static and dynamic safety regions are identified. An alert status generation algorithm is offered based on a fault tree, allowing automatic selection of the preferable emergency response strategy for a dynamically positioned vessel of class 2 and in compliance with the onboard ASOG document. A motion planning algorithm is suggested, taking into account the specific requirements of a 500-m safety zone. The generated trajectory is subject to speed and heading constraints that depend on the environmental disturbance. An overall structure of the algorithm is presented in the flowchart of Appendix B.

A part of the above proposals has been implemented industrially in the DP SafeWatch software, which is a decision support tool. Further research is aimed at collision avoidance with moving targets and at incorporating the point cloud data from detection and ranging sensors. An anonymized human-operated maneuver database acquired from DP SafeWatch is considered to be a viable reference for developing and testing unmanned vessel maneuvering strategies for offshore marine supply operations.

Glossary

ASOG	Activity specific operating guideline
CAM	Critical activity mode
COG	Course over the ground
DP	Dynamic positioning
FTA	Fault tree analysis
HDG	Heading
LOS	Line-of-sight
MSD	Minimal safety distance
OSV	Offshore support vessel
PRS	Position reference system
SOG	Speed over the ground
Stbd	Starboard
STW	Speed through the water
Thr, THR	Thruster
UTM	Universal transversal mercator projection
WCF	Worst case failure

Appendix A
Coordinate Systems and Their Transformation

Universal Transverse Mercator projection is to be used as the preferred mean of reducing the distortions and alignment with the field seismic survey charts.

Local coordinate systems are in use to produce local maps and to detect a crossing of the relevant geographic areas. For example, offshore maps can be in Nahrwan 1967 Datum UTM zone 39 N, Clarke 1880 ellipsoid, while GPS works in WGS-84 ellipsoid Latitude Φ and Longitude λ coordinates. Any local coordinates can be converted using the following sequence of transformations:

1) UTM (specified zone) to local ellipsoid [55] with following parameters: number of zone, false easting, false northing, local ellipsoid a semimajor axis of the local geodetic datum ellipsoid, b, e.
2) Local ellipsoid to WGS-84 [55] with following parameters: ΔX, ΔY, ΔZ shifts between centers of the local geodetic datum and WGS-84 ellipsoid and a, b, c of both ellipsoids.

For most applications involving maps, charts, navigation and geospatial information, a transformation of a Local Geodetic Datum to WGS-84 Datum is required. This transformation can be performed in curvilinear (geodetic) coordinates

$$\Phi_{\text{WGS}-84} = \Phi_{\text{local}} + \Delta\Phi$$

$$\lambda_{\text{WGS}-84} = \lambda_{\text{local}} + \Delta\lambda$$

where $\Delta\Phi$, $\Delta\lambda$ in seconds are

$$\begin{aligned}\Delta\Phi = \{&-\Delta X \sin\Phi\cos\lambda - \Delta Y \sin\Phi\sin\lambda + \Delta Z\cos\Phi \\ &+ \Delta a(R_N e^2 \sin\Phi\cos\Phi)/a \\ &+ \Delta f[R_M \frac{a}{b} + R_N \frac{b}{a}]\sin\Phi\cos\Phi\} \\ &\times [(R_M + h)\sin 1'']^{-1}\end{aligned}$$

$$\Delta\lambda = [-\Delta X \sin\lambda + \Delta Y\cos\lambda][(R_N + h)\cos\Phi\sin 1'']^{-1}$$

where h is the geodetic height. R_N is the radius of curvature in the prime vertical

$$R_N = a/(1 - e^2\sin^2\Phi)^{1/2}.$$

R_M stands for the radius of curvature in the meridian

$$R_M = a(1 - e^2)/(1 - e^2\sin^2\Phi)^{3/2}.$$

Appendix B
Algorithm Flowchart

See Fig. 31 for an overview of the safe maneuver planning algorithm.

Acknowledgment

This article has been produced and financed within the framework of the Smart Shipping program of BOURBON Marine and Logistics SASU. The program is deployed on a vast fleet of OSVs globally and aims at ensuring safer, more efficient, and rationalized operations.

References

[1] "United nations convention on the law of the sea," United Nations, Tech. Rep., 1982. [Online]. Available: www.un.org
[2] *Guidelines for Vessels With Dynamic Positioning (DP) Systems*, Maritime Safety Committee Circular, Int. Maritime Org., IMO MSC/Circ.645, Jun. 1994. [Online]. Available: www.imo.org
[3] *Guidelines for Vessels and Units With Dynamic Positioning (DP) Systems*, Maritime Safety Committee Circular, Int. Maritime Org., IMO MSC.1/Circ.1580, Jun. 2017.
[4] "Guidelines for offshore marine operations," Mar. Saf. Forum, Tech. Rep., 2020, Accessed: Dec. 18, 2020. [Online]. Available: http://g-omo.info/wp-content/uploads/2020/11/GOMO-Complete-Document-February-2020.pdf
[5] *Guidance on Operational Activity Planning*, Int. Marine Contractors Assoc., IMCA M. 220 Rev. 1, Dec. 2017. [Online]. Available: www.imca-int.com
[6] *International Guidelines for the Safe Operation of Dynamically Positioned Offshore Supply Vessels*, Int. Marine Contractors Assoc., IMCA 182 MSF Rev. 3, Nov. 2018. [Online]. Available: www.imca-int.com
[7] "DP operations guidance part 2 appendix 3 logistics vessels ver 2.0," Marine Technol. Society Dyn. Positioning Committee, MTS, Jul. 2012. [Online]. Available: www.dynamic-positioning.com/
[8] "Marine operations: 500 m safety zone," Step Change in Safety, Tech. Rep., Mar. 2017. [Online]. Available: https://www.stepchangeinsafety.net/resources/marine-operations-500m-safety-zone/
[9] S. Zhang, P. T. Pedersen, and H. Ocakli, "Collisions damage assessment of ships and jack-up rigs," *Ships Offshore Structures*, vol. 10, no. 5, pp. 470–478, 2015.
[10] S. Zhang and P. T. Pedersen, "A method for ship collision damage and energy absorption analysis and its validation," *Ships Offshore Struct.*, vol. 12, no. sup1, pp. S11–S20, 2017.
[11] J.-E. Vinnem, *Offshore Risk Assessment vol 1: Principles, Modelling and Applications of QRA Studies*. Berlin, Germany: Springer, 2014.
[12] *Offshore Standard: Safety Principles and Arrangements*, DNV GL AS, DNVGL-OS-A101-OS-A101, Jul. 2015.
[13] A. J. Sørensen, "A survey of dynamic positioning control systems," *Annu. Rev. Control*, vol. 35, no. 1, pp. 123–136, 2011.
[14] T. Fossen, *Marine Control Systems—Guidance. Navigation, and Control of Ships, Rigs and Underwater Vehicles*. Trondheim, Norway: Marine Cybernetics AS, 2002.
[15] A. Loria, T. I. Fossen, and E. Panteley, "A separation principle for dynamic positioning of ships: Theoretical and experimental results," *IEEE Trans. Control Syst. Technol.*, vol. 8, no. 2, pp. 332–343, Mar. 2000.
[16] T. I. Fossen and T. Perez, "Kalman filtering for positioning and heading control of ships and offshore rigs," *IEEE Control Syst. Mag.*, vol. 29, no. 6, pp. 32–46, Dec. 2009.
[17] M. Blanke and T. Nguyen, "Fault tolerant position-mooring control for offshore vessels," *Ocean Eng.*, vol. 148, pp. 426–441, 2018.
[18] *Dynamic Positioning Assurance Framework Risk-Based Guidance*, Oil Comp. Int. Marine Forum, London, U.K., 2016. [Online]. Available: https://www.ocimf.org/document-libary/dp-failure-mode-effects-analysis-assurance-framework-risk-based-guidance
[19] R. Wright, *Unmanned and Autonomous Ships: An Overview of Mass*. Abingdon, U.K.: Routledge, 2020.
[20] "Guidelines for the design and operation of dynamically positioned vessels," *Int. Mar. Contractors Assoc.*, IMCA M. 103 Rev.4.1, Oct. 2020. [Online]. Available: www.imca-int.com
[21] M. Rausand, A. Barrosa, and A. Hoyland, *System Reliability Theory: Models, Statistical Methods, and Applications*, 3rd ed. Hoboken, NJ, USA: Wiley, Nov. 2020.
[22] K. Zhou, G. Huang, S. Wang, and K. Fang, "Research on transportation safety of hazardous chemicals based on fault tree analysis (FTA)," in *Proc. 9th Int. Conf. Ind. Technol. Manage.*, 2020, pp. 206–209.
[23] C. He, R. Wang, L. Ma, X. Li, X. Jiao, and L. Song, "Research on fault diagnosis method based on FMEA/FTA and Bayesian network," in *Proc. Int. Conf. Sensing, Diagnostics, Prognostics, Control*, 2019, pp. 173–177.
[24] F. Wang, M. Lv, and F. Xu, "Design and implementation of a triple-redundant dynamic positioning control system for deepwater drilling rigs," *Appl. Ocean Res.*, vol. 57, pp. 140–151, 2016.
[25] H. Xu, G. Li, and J. Liu, "Reliability analysis of an autonomous underwater vehicle using fault tree," in *Proc. IEEE Int. Conf. Inf. Automat.*, 2013, pp. 1165–1170.
[26] A. Vagale, R. Oucheikh, R. T. Bye, O. L. Osen, and T. I. Fossen, "Path planning and collision avoidance for autonomous surface vehicles II: A comparative study of algorithms," *J. Mar. Sci. Technol.*, vol. 26, pp. 1307–1323, Jun. 2021. [Online]. Available: https://www.researchgate.net/publication/341481377
[27] Y. Cheng and W. Zhang, "Concise deep reinforcement learning obstacle avoidance for underactuated unmanned marine vessels," *Neurocomputing*, vol. 272, pp. 63–73, 2018.
[28] J. Song, C. Hao, and J. Su, "Path planning for unmanned surface vehicle based on predictive artificial potential field," *Int. J. Adv. Robot. Syst.*, vol. 17, no. 2, Mar./Apr. 2020, Art. no. 1729881420918461.
[29] E. Serigstad, B.-O. H. Eriksen, and M. Breivik, "Hybrid collision avoidance for autonomous surface vehicles," *IFAC-PapersOnLine*, vol. 51, no. 29, pp. 1–7, 2018.

[30] H. Niu, Y. Lu, A. Savvaris, and A. Tsourdos, "Efficient path planning algorithms for unmanned surface vehicle," *IFAC-PapersOnLine*, vol. 49, no. 23, pp. 121–126, 2016.

[31] V. Roberge, M. Tarbouchi, and G. Labonte, "Comparison of parallel genetic algorithm and particle swarm optimization for real-time UAV path planning," *IEEE Trans. Ind. Inform.*, vol. 9, no. 1, pp. 132–141, Feb. 2013.

[32] Y. Liu, W. Liu, R. Song, and R. Bucknall, "Predictive navigation of unmanned surface vehicles in a dynamic maritime environment when using the fast marching method," *Int. J. Adapt. Control Signal Process.*, vol. 31, no. 4, pp. 464–488, Apr. 2017.

[33] X. Sun, G. Wang, Y. Fan, D. Mu, and B. Qiu, "An automatic navigation system for unmanned surface vehicles in realistic sea environments," *Appl. Sci.*, vol. 8, no. 2, 2018, Art. no. 193.

[34] P. Medyna and M. Maka, "Determination of the shortest path as the basis for examining the most weather favorable routes," *Zeszyty Naukowe*, vol. 32, no. 104, pp. 29–33, 2012.

[35] E. S. Ueland, R. Skjetne, and A. R. Dahl, "Marine autonomous exploration using a LiDar and SLAM," in *Proc. 36th Int. Conf. Ocean, Offshore Arctic Eng.*, vol. 6, 2017, doi: 10.1115/omae2017-61880.

[36] J.-M. Yang, C.-M. Tseng, and P. Tseng, "Path planning on satellite images for unmanned surface vehicles," *Int. J. Nav. Archit. Ocean Eng.*, vol. 7, pp. 87–99, 2015.

[37] S. Gu*et al.*, "A motion planning method for unmanned surface vehicle in restricted waters," *J. Eng. Maritime Environ.*, vol. 234, no. 2, pp. 332–345, 2020.

[38] G. Li, H. Hildre, and H. Zhang, "Toward time-optimal trajectory planning for autonomous ship maneuvering in close-range encounters," *IEEE J. Ocean. Eng.*, vol. 45, no. 4, pp. 1219–1234, Oct. 2020.

[39] R. Skjetne, "The maneuvering problem," Ph.D. dissertation, Dept. Eng. Cybern., Norwegian Univ. of Sci. and Technol., Trondheim, Norway, 2005.

[40] I. Maslov, "Approach planning to marine assets (in Russian)," *Morskoy Vestnik*, vol. 1, no. 61, pp. 113–116, 2017.

[41] A. Vagale, R. T. Bye, and O. L. Osen, "Evaluation of path planning algorithms of autonomous surface vessels based on safety and collision risk assessment," in *Proc. Glob. Oceans, Singapore-U.S. Gulf Coast*, 2020, vol. SG4, pp. 1–8.

[42] N. A. Jenssen, "What is the DP current," in *Proc. Dyn. Positioning Conf.*, Oct. 2006, Art. no. 11. [Online]. Available: https://dynamic-positioning.com/proceedings/dp2006/control_jenssen.pdf

[43] B. Kinsman, *Wind Waves: Their Generation and Propagation on the Ocean Surface*. Englewood Cliffs, NJ, USA: Prentice-Hall, 1965.

[44] *Guidance on Position Reference Systems and Sensors for DP Operations*, Int. Marine Contractors Assoc., IMCA M. 252 Rev. 0.1, Dec. 2020. [Online]. Available: www.imca-int.com

[45] "Wartsila RS24 brochure," Wartsila Guidance Marine, Tech. Rep., Accessed: Jan. 2, 2021. [Online]. Available: https://www.wartsila.com/docs/default-source/voyage/94-0486-4-d-rs24-handout.pdf?Status=Master&sfvrsn=d14b6543_7/94-0486-4-D-RS24-Handout.pdf

[46] "Wartsila SceneScan brochure," Wartsila Guidance Marine, Tech. Rep., Accessed: Jan. 2, 2020. [Online]. Available: https://www.wartsila.com/docs/default-source/voyage/94-0486-4-d-scenescan-handout.pdf?Status=Master&sfvrsn=1c2b6543_3/94-0486-4-D-SceneScan-Handout.pdf

[47] *Assessment of Station Keeping Capability of Dynamic Positioning Vessels*, DNV GL AS, DNVGL-ST-0111 -ST-0111, Jul. 2016.

[48] *DP Failure Mode Effects Analysis Assurance Framework Risk-Based Guidance*, Oil Companies Int. Marine Forum, London, U.K., 2020.

[49] "DP station-keeping bulletin," Int. Marine Contractors Assoc., IMCA DPE 04/19, Nov. 2019. [Online]. Available: www.imca-int.com

[50] "DP station-keeping bulletin," Int. Marine Contractors Assoc., IMCA DPE 03/15, Aug. 2015. [Online]. Available: www.imca-int.com

[51] S. LaValle, *Planning Algorithms*. Cambridge NY, USA: Cambridge Univ. Press, 2006.

[52] "DP station-keeping bulletin," Int. Marine Contractors Assoc., IMCA DPE 01/20, Feb. 2020. [Online]. Available: www.imca-int.com

[53] "NavDP4000 series dynamic positioning systems," *Navis Eng. OY, Tech. Rep.*, Accessed: Jan. 2, 2020. [Online]. Available: https://navisincontrol.com/upload/iblock/3e3/Nav_DP_brochure.pdf

[54] T. Fossen, M. Breivik, and R. Skjetne, "Line-of-sight path following of underactuated marine craft," *IFAC Proc. Vol.*, vol. 36, pp. 211–216, 2003.

[55] *User's Handbook on Datum Transformations Involving WGS 84*, Int. Hydrographic Bureau Monaco, Monte Carlo, Monaco, Jul. 2003.

Ilia Maslov (Member, IEEE) received the B.S. and M.S. degrees in navigation from Admiral Makarov State Maritime Academy, Saint Petersburg, Russia, in 2011.

He started his career as a Mariner (2011–2017). Since 2017, he has been working as a Fleet Dynamic Positioning Expert and Superintendent with BOURBON Offshore Head Office, Marseille, France, and also as a Project Manager for marine remote surveillance, decision support, and digital redundancy testing projects. His research interests include FMEA, functional safety, and maneuvering control and optimization.

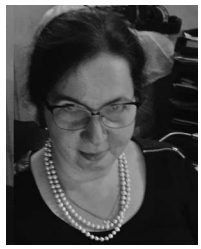

Elena B. Ambrosovskaya received the B.S. and M.Sc. degrees in mechanics and control processes from St. Petersburg Polytechnical University, Saint Petersburg, Russia, in 1995, and the Ph.D. degree in systems of information processing and control from St. Petersburg Electrical Engineering University, Saint Petersburg, in 1998.

Since 1994, she has been working as a Senior Researcher with Navis Engineering Oy, Vantaa, Finland.

Alexander M. Dvorkin received the B.S. and M.S. degrees in mechanics and control processes from St. Petersburg Polytechnical University, Saint Petersburg, Russia, in 1995.

From 1994 to 2000, he was a Senior Researcher with Navis Engineering Oy, Vantaa, Finland, in the Ship Motion Simulation Department and now in the Dynamic Positioning Systems Department.

Anton V. Proskurnikov (Senior Member, IEEE) received the M.Sc. and Ph.D. degrees in applied mathematics from St. Petersburg State University, Saint Petersburg, Russia, in 2003 and 2005, respectively.

He is an Associate Professor with the Department of Electronics and Telecommunications, Polytechnic of Turin, Turin, Italy. Previously, he was an Assistant Professor with St. Petersburg State University (2003–2010), a Deputy Chief Engineer with Navis Engineering Oy (2007–2013), a Postdoctoral Researcher with the University of Groningen (2014–2016), and the Delft University of Technology (2016–2018). He is an Associate Editor for IEEE TRANSACTIONS ON AUTOMATIC CONTROL. His research interests include nonlinear control, multiagent systems, and complex networks.

Alexander Mordvintsev received the B.S. and M.S. degrees in instrument engineering and the M.S. degree in management of information systems from St. Petersburg State Polytechnical University, Saint Petersburg, Russia, in 2005 and 2010, respectively.

He started his career in hydroacoustic, and continued in the development of navigation systems. Since 2013, he has been with the DP Projects Department, Navis Engineering Oy, Vantaa, Finland, where he is currently in charge of new product development in the area of maneuver control systems.